Title
Power Transfer Techniques for Biomedical Implants

Author
Anwar, Usama

Publication Date
2021

Peer reviewed|Thesis/dissertation

University of California
Los Angeles

Power Transfer Techniques for Biomedical Implants

A dissertation submitted in partial satisfaction
of the requirements for the degree
Doctor of Philosophy in Electrical and Computer Engineering

by

Usama Anwar

2021

Abstract of the Dissertation

Power Transfer Techniques
for Biomedical Implants

by

Usama Anwar
Doctor of Philosophy in Electrical and Computer Engineering
University of California, Los Angeles, 2021
Professor Dejan Markovic, Chair

Biomedical implants are designed to last inside the human body for more than a decade. Critical to the longevity of the implants is how power is distributed inside the implant. The first part of the thesis explores how wired power is efficiently delivered inside a distributed implant. AC power must be delivered to avoid tissue polarization. Furthermore, the frequency should be high to reduce the size of rectification capacitors on power receivers. A T-LCC resonant converter topology is presented that can deliver wired AC power efficiently at high frequency while achieving high efficiency.

Distributed implants involve multiple stages of power conversion, all of which introduce losses. Furthermore, the implants must be connected through leads, which involve extra surgeries and are inconvenient. For example traditional lead-based cardiac pacemakers suffer from lead-related complications which include lead fracture, lead dislodgement, and venous obstruction. Modern leadless pacemakers mitigate the complications, but, since they are implanted inside the heart with a small battery, their limited battery lifetime necessitates device replacement. The second part of my thesis presents a leadless and batteryless, wirelessly powered intravenous cardiac pacemaker that mitigates both problems. The pacemaker has a passive wireless power receiver (RX) circuit that receives bursts of power from a transmitter (TX) and stimulates the tissue. The circuit applies monophasic, cathodic, and current/voltage stimulation to the heart with a programmable pulse period. It consumes

1mW power for a 0.5msec stimulation pulse, which qualifies for pacemaker application. A 5V voltage and 5mA current stimulation over 3cm TX and RX distance with controllable pulse width and pulse frequency is demonstrated. In-vivo device characterization demonstrates the potential of the device to advance pacemaker technology.

The cardiac pacemaker has a very small form factor and is implanted in a greater cardiac vein, which is wirelessly powered by a subcutaneous module. The subcutaneous module includes a rechargeable battery and is powered once in a few months from an external module. The third part of this thesis presents a wireless power transfer system (WPT) for power transfer between external and subcutaneous modules. Power is transmitted in bursts between the external transmitter and subcutaneous receiver modules. The duty cycle of the burst is controlled through load modulation to control power flow between the modules. The proposed WPT circuit can regulate output voltage against distance and load variations. No extra communication channel is present to establish feedback between transmitter and receiver, making the circuit suitable for many applications. A 330-milliwatt prototype circuit for use in a pacemaker application is demonstrated.

The dissertation of Usama Anwar is approved.

Nanthia Suthana

Subramanian Iyer

Asad Abidi

Dejan Markovic, Committee Chair

University of California, Los Angeles

2021

To my parents, Samina Anwaar and Anwar ul Haq

Table of Contents

List of Figures

List of Tables

Acknowledgments

I want to thank Prof. Dejan Markovic for his guidance and support during my Ph.D. He provided invaluable support and guidance throughout my research. I have greatly benefited from him and remain thankful to him for his mentorship.

I want to thank Prof. Asad Abidi and Prof. Sudhakar Pamarti for their courses. I have learned a lot about circuit design from the coursework, and it has helped me in my research.

I want to thank Adrian Tang and Hameed Rahmani for helping me in designing my first chip and teaching me a lot about the technology. Furthermore, I thank Chemy Amir and Mohammad Mahdi from Analog Bits. They took time to supervise me and taught me a lot about circuit design.

I thank Prof. Kalyanam Shivkumar, Prof. Olumjimi Ajijola, and their team for helping with the animal experiments and their promptness in arranging such experiments. The experiments helped in getting animal experiment results in the pacemaker project.

I thank Star Li, Ali Reza Yousefi, Uneeb Rathore, Sumeet Nagi, Wenhao Yu, and Jiacheng Pan for discussing ideas. Zhaoyi Louis's help in designing a test board used is testing and characterizing electrodes, and his assistance in the wireless power transfer project is very much appreciated.

I am thankful to my family. My wife, Fatima Sajid, was tremendous support and helped me in the pacemaker project. Her knowledge of medicine made it much easier for me to discuss the project with her and get good ideas on the pacemaker clinical use. She also assisted during the animal experiments. Finally, I can not thank enough my parents, Samina Anwaar and Anwar ul Haq, for their continued support throughout my Ph.D.

Vita

2014 B.S. (Electrical Engineering), Lahore University of Management Sciences (LUMS), Lahore, Pakistan.

2016 M.S. (Electrical Engineering), University of Colorado, Boulder.

Publications

U. Anwar , O. A. Ajijola, K. Shivkumar, and D. Markovic, " Towards a Leadless Wirelessly Controlled Intravenous Cardiac Pacemaker ," IEEE Transactions on Biomedical Circuits and Systems. (Submitted)

U. Anwar, Z. Louis, and D. Markovic, "A 6.78 MHz Burst-Mode Controlled Inductive Wireless Power Transfer System," IEEE Transactions on Power Electronics. (Submitted)

U. Anwar, Z. Louis, and D. Markovic, "A Burst Mode Controlled Inductive Wireless Power Transfer System," Proceedings of the IEEE Workshop on Control and Modeling for Power Electronics (COMPEL), Aalborg, Denmark, 2020.

U. Anwar, and D. Markovic, "Dynamic Modelling of Hybrid Feedforward Controlled Pulse Width Modulated Switching Converters," Proceedings of the IEEE Workshop on Control

and Modeling for Power Electronics (COMPEL), Aalborg, Denmark, 2020.

U. Anwar, K.K. Afridi, and D. Markovic, "High-Frequency Resonant Inverter for Power Transfer Between Distributed Modules of a Biomedical Implant," Proceedings of the IEEE Energy Conversion Congress and Exposition (ECCE), Baltimore, MD, September 2019.

CHAPTER 1

Introduction

Biomedical implants are widely employed to extend and improve quality of life, and their adoption can potentially grow with improvements in technology. Implants are designed to last more than a decade. Therefore, energy storage and power distribution are critical in implants. Furthermore, biomedical implants have a small form factor to conveniently fit inside the body that further constrains the battery size. An implant lifetime can be extended by using a rechargeable battery and wirelessly charging it. Patients can have movement while wearing an external charger. Furthermore, it becomes difficult to align the external charger with the implant. Therefore, a wireless charger must be designed to exhibit immunity to distance and load variations.

An implant lifetime can also be extended by using wireless power transfer technology for mitigating leads in implants. Leads can develop complications that necessitate device replacement. Therefore, eliminating leads could reduce complications and extend implant lifetime.

This thesis contributes to three areas that relate to power distribution and transfer to a biomedical implant.

1.1 Wired power transfer between distributed modules of a biomedical implant

The first part of the thesis discusses considerations of wired power transfer between distributed modules of a biomedical implant. Power must be transferred as AC between dis-

tributed modules to avoid tissue polarization. The cable must appear electrically neutral to the body. A resonant inverter architecture is proposed for wired power transfer between distributed modules of a biomedical implant. The proposed inverter comprises a full-bridge inverter and two T-LCC resonant networks that help generate the required ac output voltage. It is demonstrated that this T-LCC resonant inverter topology can maintain near-constant output voltage across a wide load range without closed-loop control. The proposed inverter can also achieve high efficiency by minimizing circulating losses and maintaining soft switching across a wide load range. A 130mW, 1MHz prototype T-LCC resonant inverter achieves a full power efficiency of 86% and maintains efficiency above 80% across a two-to-one power range. Furthermore, the converter achieved a power density of $12W/in^3$.

A distributed implant is comprised of multiple stages of power conversion all of which can introduce losses in the system power delivery. Furthermore, leads in a distributed implant can have short- and long-term complications. Therefore, mitigating the leads by transferring wireless power to the implant could promote implant adoption. Cardiac pacemakers, in particular, can greatly benefit from wireless power transfer technology.

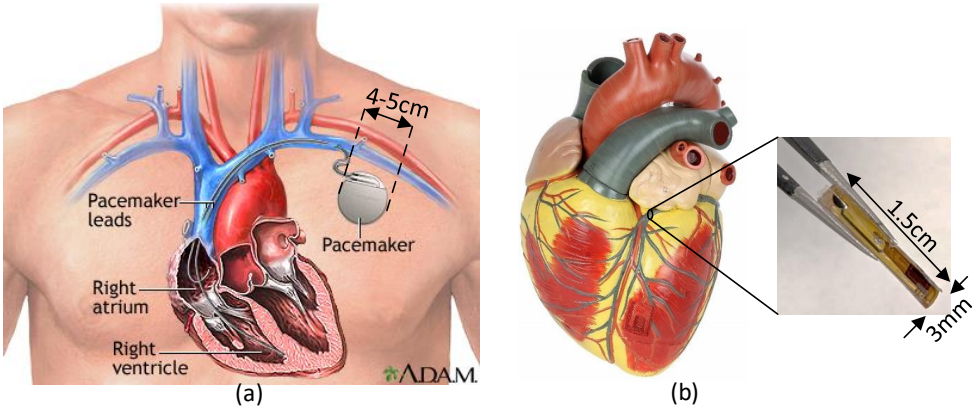

Figure 1.1: (a) Traditional pacemaker and (b) proposed pacemaker.

1.2 Leadless and batteryless wirelessly powered intravenous cardiac pacemaker

The second part of the thesis introduces a leadless and batteryless intravenous cardiac pacemaker. Traditional lead-based cardiac pacemakers, shown in Fig. 1.1, suffer from lead-related complications which include lead fracture, lead dislodgement, and venous obstruction. Modern leadless pacemakers mitigate the complications, but, since they are implanted inside the heart with a small battery, their limited battery lifetime necessities device replacement within the patient's lifetime. This thesis presents a leadless and batteryless, wirelessly powered intravenous cardiac pacemaker that mitigates both problems. The pacemaker uses a passive wireless power receiver (RX) circuit that receives bursts of power from a transmitter (TX) and stimulates the tissue. The pulse period of the burst is controlled to stimulate the myocardium and the frequency is controlled to regulate the heartbeat. The TX power consumption is significantly reduced by turning it on only for the duration the stimulation is applied. The RX is designed to accurately detect the pulse period of TX and stimulate the heart only for that duration. A rectifier is proposed that allows 5V stimulation to cover broad range of patients. After stimulation, the RX circuit shorts electrodes to neutralize the injected charge. A large decoupling capacitor commonly used in charge neutralization circuits is avoided to minimize implant electronics.

The circuit applies monophasic, cathodic, and current/voltage stimulation to the heart with a programmable pulse period. It consumes 1mW power (for a 0.5msec stimulation pulse), which allows the pacemaker to operate for 5 months using a 1Ah rechargeable battery. A 5V voltage stimulation and 5mA current stimulation over 3cm TX and RX distance with controllable pulse width and pulse frequency is demonstrated. The pacemaker functionality was verified in-vivo in a porcine model by increasing the heartbeat from 64bpm to 100bpm.

The cardiac pacemaker is comprised of multiple modules as shown in Fig. 1.2. Stimulation

module is located in a cardiac vein. It is powered wirelessly from the subcutaneous module which contains a rechargeable battery. The battery is recharged once in a few months from an external module. Wireless power transfer between external and subcutaneous module needs to exhibit immunity to distance and load variation. Furthermore, it should achieve high efficiency and transmit power in a standard ISM band.

1.3 Wireless power transfer for a biomedical implant

The third part of the thesis introduces a burst-mode controlled inductive wireless power transfer system that exhibits immunity to distance and load variations. Power is transmitted at a constant frequency in bursts between the transmitter (TX) and receiver (RX) such that TX only transmits power for the time RX needs it. The duty cycle of the burst is controlled through load modulation to control power flow between TX and RX. The proposed WPT circuit exhibits immunity to distance up to 3cm TX-RX separation and load variations from full load to no load. No extra communication channel is present to establish feedback between transmitter and receiver. A 330mW prototype circuit to charge a 280mAh battery for use in a medical implant is designed, built, and tested.

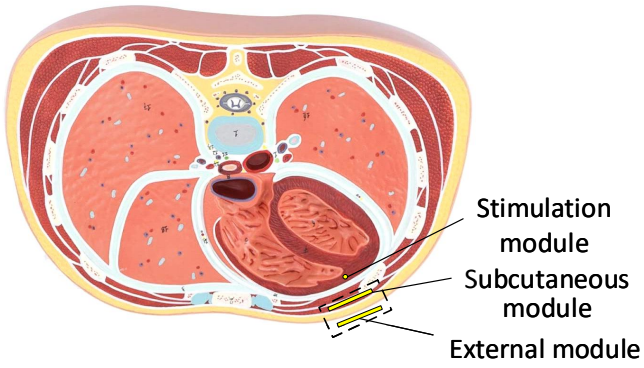

Figure 1.2: Pacemaker system architecture.

1.4 Thesis outline

Circuit for wired power transfer between distributed modules of an implant is presented in Chapter 2. Chapter 3 presents as a leadless and batteryless, wirelessly powered intravenous cardiac pacemaker. Wireless power transfer for biomedical implants is discussed in Chapter 4. Finally, Chapter 5 concludes the thesis by presenting a summary of research contributions and future work.

CHAPTER 2

High-Frequency Resonant Inverter for Power Transfer Between Distributed Modules of a Biomedical Implant

Biomedical implants are widely employed to extend and improve quality of life, and their adoption can potentially grow with improvements in technology. To evaluate the effect of new sensing and stimulation technologies on the clinical efficacy of implants, researchers sometimes use modular architecture to test various features, as done in the case of deep brain stimulation (DBS) system shown in Fig. 2.1(a) [7, 8]. The modules are interconnected by implantable cables. This architecture is extended from a traditional chest-based system with passive leads, as shown in Fig. 2.1(b) [9]. The traditional system has a single battery in the chest module, which can be wirelessly recharged from an external source [10]. Extending this approach to the modular implant, power has to be distributed as ac to avoid tissue polarization [11]. Even with ac power, it is desirable that the dc component of the voltage between each conductor and the dc ground be zero, so the power is transferred using two 180°phase-shifted ac voltages, as shown in Fig. 2.2. In this manner, there is no electric field

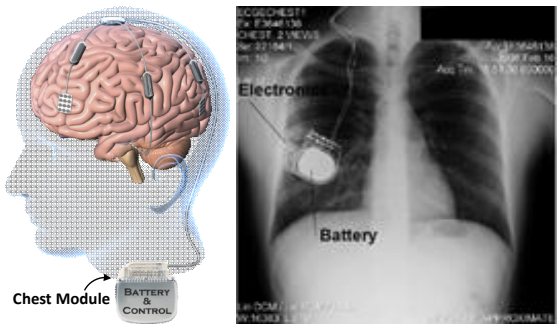

Figure 2.1: (a) Structure of a modular research DBS device, extended from a traditional chest-based device and (b) commercial implanted DBS device.

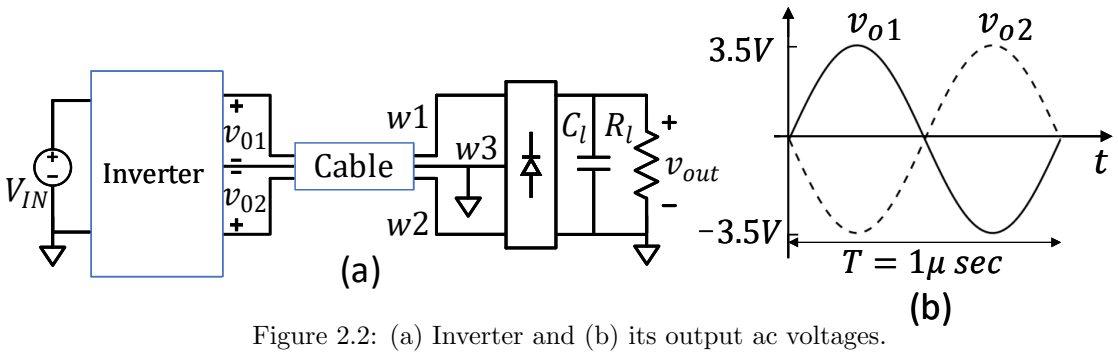

Figure 2.2: (a) Inverter and (b) its output ac voltages.

between cable and the body across the length of the cable and the cable appears electrically neutral to the body. Furthermore, in case of short circuit between circuit ground and body, the current flowing between the modules returns through the two ac power lines rather than through the body.

In ac power distribution, the modules receiving the power rectify and filter the ac voltage. These battery-free modules are size-constrained with connectors and electronics, so it is highly desirable to reduce the size of the filtering capacitors by utilizing high-frequency ac. Hence, there is a need in the power source module for a high-frequency small-form-factor inverter which produces at its two output terminals dc-neutral ac voltages.

This chapter presents a resonant inverter architecture appropriate for wired power transfer between distributed modules of a biomedical implant. The proposed inverter generates ac voltages without any dc components at its two output terminals. In addition, the T-LCC resonant converter topology introduced in this chapter can regulate output voltage across large variations in load without the need for closed-loop control. This is extremely valuable, as it eliminates sensing and control circuitry, including a potentially always-active microcontroller, and eases size and energy constraints. The proposed inverter can also achieve high efficiency by minimizing circulating current losses and maintaining soft switching across a wide load range. A 130-mW, 1-MHz prototype of the proposed resonant inverter achieves a full-power efficiency of 86% and maintains efficiency above 80% across a two-to-one power range.

Table 2.1: DESIGN SPECIFICATIONS OF THE INVERTER.

Parameter	Value
Input voltage (V_{IN})	3.6 V
Output voltage ($v_{o1,2}$)	3.6 V_{pk}
Output power	0-130mW
Frequency (f_s)	1MHz
Voltage conversion ratio	$\frac{3.5}{(\frac{2}{\pi})3.6}$

2.1 System and inverter architecture

The ac power delivery architecture needed for the modular biomedical implant is shown in Fig. 2.2(a), and its inverter specifications are listed in Table 2.1. The inverter and rectifier are typically connected by a multi-conductor cable, but only the three conductors relevant to power delivery are shown in Fig. 2.2(a). Conductors w1 and w2 connect the two output terminals of the inverter to the two input terminals of the rectifier. Conductor w3 connects the ground of the inverter to the ground of the rectifier. The dc components of the three voltages between these conductors are required to be zero. This can be achieved using an inverter that produces the two 180°out-phased ac voltages shown in Fig. 2.2(b).

One approach evaluated for the architecture of the inverter converts dc voltage to high-frequency ac using a square-wave full-bridge inverter, and then uses a center-tap transformer

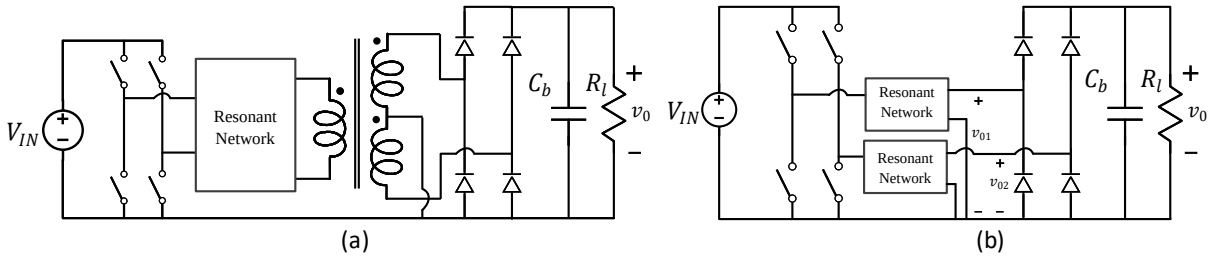

Figure 2.3: Two possible architectures for the required dc-ac power conversion: (a) using a full-bridge resonant inverter and a center-tapped transformer, and (b) using two 180°-phase-shifted half-bridge inverters and two appropriately selected resonant networks.

to generate the two 180°-phase-shifted ac voltages, as shown in Fig. 2.3(a). This inverter architecture also utilizes a high-Q resonant tank to filter out the high-frequency harmonics and produce a near-sinusoidal output. This approach has a number of drawbacks for the considered application. The transformer introduces significant winding and core losses at 1MHz, adversely impacting conversion efficiency, which is an important metric given the limited energy available to the implant. Furthermore, the volume of the transformer is substantial, and becomes a limiting factor in this size-constrained application. Since isolation and large voltage transformation are not needed in this application, an inverter architecture that eliminates the transformer is highly desirable.

The transformer can be eliminated from the inverter by exploiting the symmetry of the circuit. The square-wave (i.e., near-50% duty-ratio) full-bridge inverter of Fig. 2.3(a) can be considered as two half-bridge inverters operating with a 180° phase shift between them. Considering each half-bridge inverter as a separate inverter, the inverter outputs can be filtered and boosted in amplitude using appropriately selected resonant tanks to generate the desired sinusoidal voltages at the two output terminals of the inverter (v_{o1}, v_{o2}), as shown in Fig. 2.3(b). The two inverters must not only maintain 180° phase shift between their respective outputs, each output must also have zero dc component. Since the output voltage of the half-bridge inverter has a non-zero dc component (value equal to $V_{IN}/2$), the resonant network used in the inverter architecture must be designed to eliminate dc component, as well as achieve the desired voltage conversion ratio and filter out high-frequency harmonics. The resonant network must also have an input impedance characteristic that minimizes circulating currents and provides zero-voltage-switching (ZVS) opportunity to the inverter switches across a range of output power.

2.2 Resonant network design

To meet the challenges of the biomedical implant application, the resonant network in the inverter architecture of Fig. 2.3(b) must be designed to achieve a small footprint and high

efficiency, while meeting the desired voltage conversion (ratio of output voltage to fundamental component of switched input voltage), filtering, and load regulation characteristics. The required voltage conversion ratio is 1.527, which means that the network must have the ability to boost voltage. The resonant network must also filter out the high-frequency harmonics present in a square wave. Good load regulation can be achieved either by sensing the output voltage and implementing feedback control, or by designing the network to have very low output impedance and simply operating the inverter in open-loop. Feedback control requires an always-on microcontroller with dedicated analog-to-digital conversion (ADC). Biomedical implants have limited energy, so microcontrollers are put in sleep mode for extended periods. Also the number of ADCs is very limited and only used for critical purposes, such as communication between modules and with external electronics. Therefore, it is desired that the inverter achieves good load regulation without feedback control. A resonant network topology with low output impedance would meet this challenge. To achieve small size, the number of inductors in the resonant network must be minimized. The load in this application is electronics stimulating the brain with current pulses. Since the brain stimulation is done sporadically, the inverter is loaded across a wide range of output power. Therefore, the inverter should be designed to achieve high efficiency over a wide range of output power.

Conventional series-LC, parallel-LC, and LCC resonant inverter topologies are unable to meet all of the above mentioned requirements simultaneously. Typical resonant network topologies have non-negligible output impedance, which causes the output voltage to drop significantly as load increases. When the parallel-LC tank is designed to achieve low output impedance, its input impedance is a weak function of load, resulting in large circulating currents and a degradation in inverter efficiency. The series-LC tank is unable to attenuate high-frequency harmonics very well due to single-pole attenuation at high frequencies.

An attractive topology for this application is the T-LCC resonant-network-based inverter shown in Fig. 2.4(a). It can simultaneously address all of the above-mentioned challenges. The topology has been identified as one of the possible three-element resonant converter topologies [12] and considered for use in automotive electronics [13, 14]. Furthermore, in

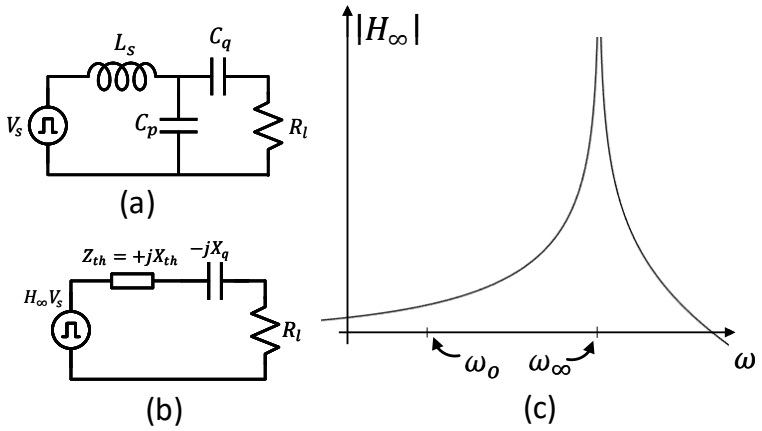

Figure 2.4: (a) T-LCC resonant network topology, (b) its Thevenin equivalent and (c) Bode plot of the converter open circuit voltage transfer function (H_∞).

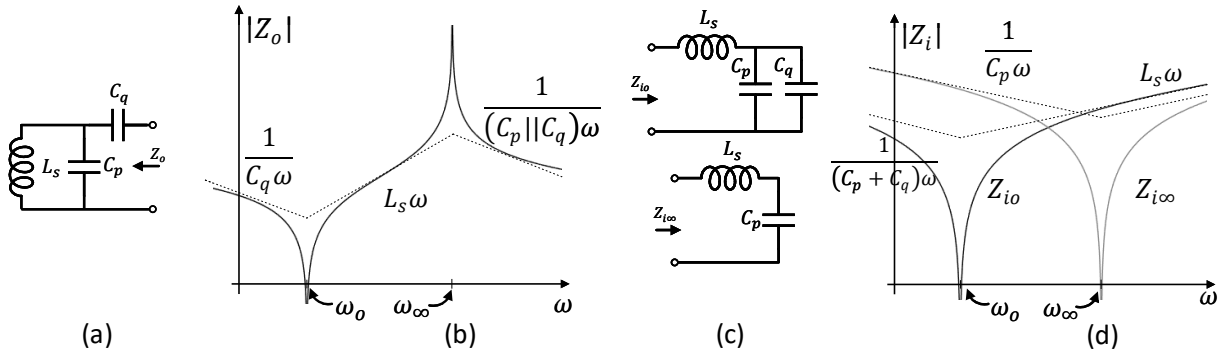

Figure 2.5: (a) Output impedance circuit and (b) its Bode plot. (c) Input impedance circuit when the output is open circuited and short circuited and (d) the corresponding Bode plots.

[13], it is identified that the converter output voltage remains regulated over variations in load without any need of feedback control circuitry for specific operating conditions (voltage gain of 2, if operated at frequency 70% of the converter resonant frequency). This paper analyzes the converter topology more generally for voltage gain greater than unity, identifies other practically useful properties of the circuit topology and presents a design criteria to choose the circuit components.

2.2.1 T-LCC topology considerations

Consider the T-LCC converter topology shown in Fig.2.4(a). Inductor L_s and capacitor C_p form a parallel resonant tank. Thevenin equivalent of the parallel resonant tank is shown in Fig. 2.4(b). Here, H_∞ is the converter open-circuit voltage gain and Z_{th} is the parallel L_sC_p tank equivalent Thevenin (output) impedance and can be expressed as:

$$H_\infty = \frac{1}{1-(\frac{\omega_s}{\omega_\infty})^2}, \tag{2.1}$$

$$Z_{th} = jX_{th} = \frac{jL_s\omega_s}{1-(\frac{\omega_s}{\omega_\infty})^2}, \tag{2.2}$$

$$\omega_\infty = \frac{1}{\sqrt{L_sC_p}}. \tag{2.3}$$

Here, ω_s is the frequency of operation and ω_∞ is the resonance frequency of parallel L_sC_p tank. If the parallel L_sC_p tank is operated below the tank resonant frequency ($\omega_s < \omega_\infty$), the converter output impedance (Z_{th}) is inductive ($+jX_{th}$). A capacitor C_q can be added in series with the tank, such that the capacitor impedance ($-jX_q$) is equal and opposite to the L_sC_p tank impedance ($+jX_{th}$) and the converter output impedance becomes zero. Thus, the converter can regulate output voltage over large variations in load in an open-loop manner. The capacitance C_q is given by:

$$C_q = \frac{1-\omega_o^2L_sC_p}{\omega_o^2L_s}. \tag{2.4}$$

Alternatively, ω_o can be expressed in terms of circuit parameters as:

$$\omega_o = \frac{1}{\sqrt{L_s(C_p+C_q)}}. \tag{2.5}$$

ω_o is the resonance frequency of inductor L_S and capacitor $(C_p + C_q)$. It is noted that ω_o is lower than ω_∞ and the converter switching frequency ω_s is chosen to be close to ω_o ($\omega_s \approx \omega_o$).

The inverter open-circuit voltage gain (H_∞) is plotted in Fig. 2.4(c) and it can be noted that the voltage gain of T-LCC resonant converter is the same as that of parallel L_sC_p tank (presence of C_q does not affect the gain). Furthermore, since the circuit is operated below the resonance frequency (ω_∞), the topology is suited for applications that require voltage gain greater than unity. Output impedance of the circuit shown in Fig. 2.5(a) is plotted in Fig. 2.5(b). It can be observed that output impedance goes to zero at ω_o. Therefore, the circuit can regulate output voltage across large load variation if it is operated at ω_o.

Another practically important feature of the topology is that circulating currents in the converter are minimized, as the topology input impedance exhibits strong dependence on the load. The converter input impedance when the output is short circuit (Z_{io}) and when the output is open circuit ($Z_{i\infty}$) are shown in Fig. 2.5(c) and plotted in Fig. 2.5(d). The two input impedances form a series resonant circuit with different resonant frequencies. If the circuit is operated at or slightly above ω_o, the converter input impedance when the output is open circuited ($Z_{i\infty}$) is significantly higher than the input impedance when the output is short circuited (Z_{io}). This implies that the resonant network's input impedance is dominated by load impedance (i.e., input currents back off as load decreases) and the inverter can achieve high efficiency over large variations in load.

Switching losses in MOSFETs can be quite significant especially for high input voltage and high operating frequency converters ($E_{sw,loss} = C_{sw}V_{in}^2 f_s$). Zero-voltage switching (ZVS) can eliminate the switching loss. ZVS for the topology can be achieved if input impedance of the circuit is inductive. As it can be observed from Fig. 2.5(d), if the converter is operated between ω_o and ω_∞, the converter input impedance transitions from inductive to capacitive as output goes from short circuit to open circuit. Critical value of the load resistance when input transitions from inductive to capacitive is given as [15]:

$$R_{crit} = \|Z_o(j\omega_s)\| \sqrt{\frac{-Z_{i\infty}(j\omega_s)}{Z_{io}(j\omega_s)}}. \tag{2.6}$$

Thus, for $R < R_{crit}$, ZVS can be achieved. Finally, the topology has only one inductor,

enabling a small size. Hence, the T-LCC resonant network topology is well-suited to address the challenges associated with wired power distribution in modular biomedical implants.

2.2.2 T-LCC resonant converter design

In the T-LCC resonant inverter, three independent design parameters (L_s, C_p, C_q) are available. To achieve the desired inverter characteristics discussed above, these parameters must be selected appropriately. The inverter specifications include an open-circuit inverter voltage gain (H_∞), an operating frequency (ω_s), and the need to achieve zero output impedance ($Z_o = 0$). The inverter open-circuit voltage gain (H_∞) depends only on L_s and C_p, as calculated in equation 2.1 and can be expressed as:

$$H_\infty = \frac{1}{1 - \omega_s^2 L_s C_p}. \tag{2.7}$$

For a given specification, equation 2.7 can be solved for the product $L_s C_p$, of which one can be chosen freely or based upon the desired loaded quality factor of the tank. With L_s selected, C_q can be chosen using equation 2.2. To get near-zero output impedance while also achieving ZVS, the inverter must be designed to operate slightly above the frequency where output impedance is zero (i.e., $\omega_s \succeq \omega_o$):

$$\omega_s \succeq \frac{1}{\sqrt{L_s(C_p + C_q)}}. \tag{2.8}$$

Note that by selecting ω_o to be close to the operating frequency (ω_s), there is a large difference between Z_{io} and $Z_{i\infty}$, leading to reduced circulating currents and improved converter efficiency over large load variations.

2.3 Proposed resonant inverter

The proposed resonant inverter is shown in Fig. 2.6. Based on the above discussion, the inverter would only comprise two 180° out-phased half bridges and two T-LCC resonant

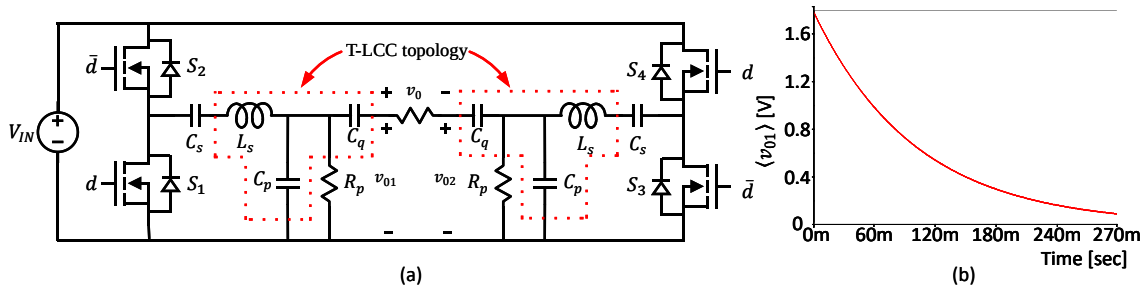

Figure 2.6: (a) Topology of the proposed resonant inverter (load represented by resistor); (b) Simulated average output voltage.

networks (L_s, C_p, C_q), with the load differentially connected across the two outputs v_{o1} and v_{o2}. However, the output voltage of each half-bridge inverter has a dc component of $V_{IN}/2$. If only an LCC resonant network is used, this dc component will appear across the capacitors C_p, and as a common-mode voltage in both outputs (v_{o1}, v_{o2}). To eliminate this dc component from the output voltages, a dc blocking capacitor C_s is added in series with inductor L_s. But even with the addition of C_s, the dc component at the output of the half-bridges will only get divided between C_s and C_p, and not be completely eliminated from the outputs (v_{o1}, v_{o2}). To ensure that the dc voltage appears solely across C_s a large resistor R_p is added in parallel with C_p. This eliminates the dc component from the output voltages (v_{o1}, v_{o2}) in periodic steady state. In periodic steady state if a dc voltage were to appear across C_p, a dc current would need to flow through R_p, which cannot happen due to the presence of C_s and C_q in the path of any dc current through R_p. Hence, no dc voltage appears across C_p and the inverter outputs (v_{o1}, v_{o2}). The circuit of Fig. 2.6(a) was simulated, and the average of the output voltage v_{o1} is shown in Fig. 2.6(b), validating that the dc component of the output voltage becomes zero in steady state. The resistance value of R_p is chosen to be large enough to have negligible losses during the converter's steady state operation.

2.4 Prototype design and experimental results

A 130mW Li-ion battery powered dc-ac converter operating at 1 MHz was designed, built and tested. Prototype of the circuit is shown in Fig. 2.7(a). Output voltage waveforms

of the converter are shown in Fig. 2.8(a) and 2.8(b) for no load and full load conditions, respectively. From the waveforms, it can be observed that the converter achieves desired voltage conversion ratio and the output voltage amplitude remains fairly constant across full load range. Switch node voltage waveform (v_{sw}) for the converter is shown in Fig. 2.7(b), from which it can be observed that there is minimal to no ringing. The voltage smoothly transitions verifying that the converter achieves ZVS. The converter achieves an efficiency of 86% at full output power (130mW) and 80% at half output power (65mW), as shown in Fig. 2.9(a). Measured output voltage across the load as a function of power drawn by the load is shown in Fig. 2.9(b). From the plot it can be observed that the output voltage remains fairly constant even with load variations. The components used in the prototype converter are listed in Table 2.2. Non-medical grade inductors were used for testing the prototype board and medical grade inductors were used in final prototype circuit shown in Fig.2.7. Medical grade inductors usually have lower Q which contribute to degradation of circuit efficiency. The final prototype achieved power density of $12W/in^3$.

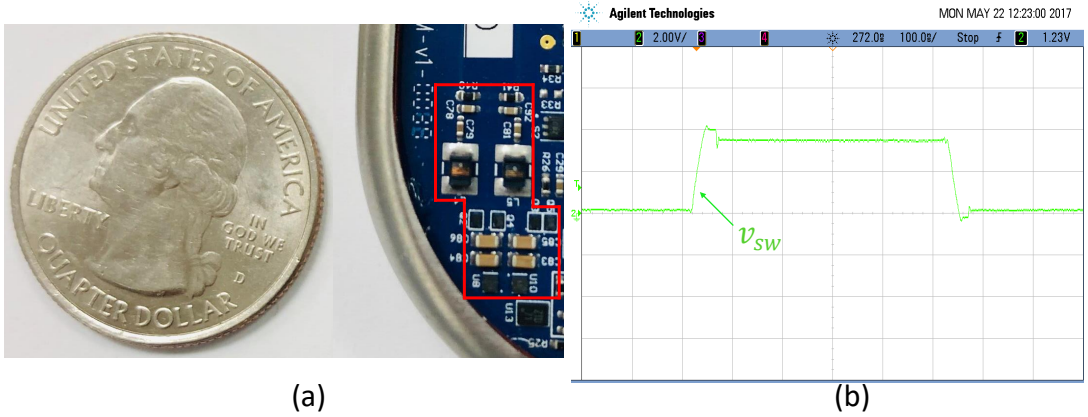

Figure 2.7: (a) Inverter prototype board and (b) Switched node voltage.

Table 2.2: COMPONENTS USED IN INVERTER.

N-Channel MOSFET (S_1, S_2)	SiUD412ED
	12 V, 340 mΩ, 0.5 A
P-Channel MOSFET (S_3, S_4)	SiUD403ED
	-20 V, 1.25 Ω, 0.5 A
Inductor (L_s)	78F3R3J-RC, 3.3 µH (non-medical grade)
	ST450PHA332KLZ, 3.3 µH (medical grade)
Capacitor (C_p, C_q, C_s)	2.67nF, 5nF,0.1 µF
Resistor (R_p)	100 kΩ
Gate Driver	NC7WZ04, NC7WZ16

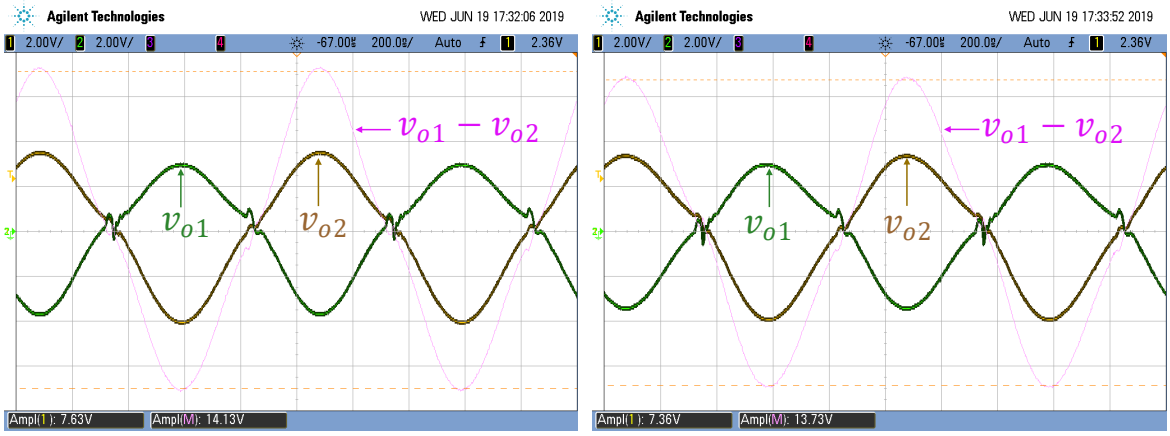

Figure 2.8: (a) No load and (b) Full load converter output waveforms.

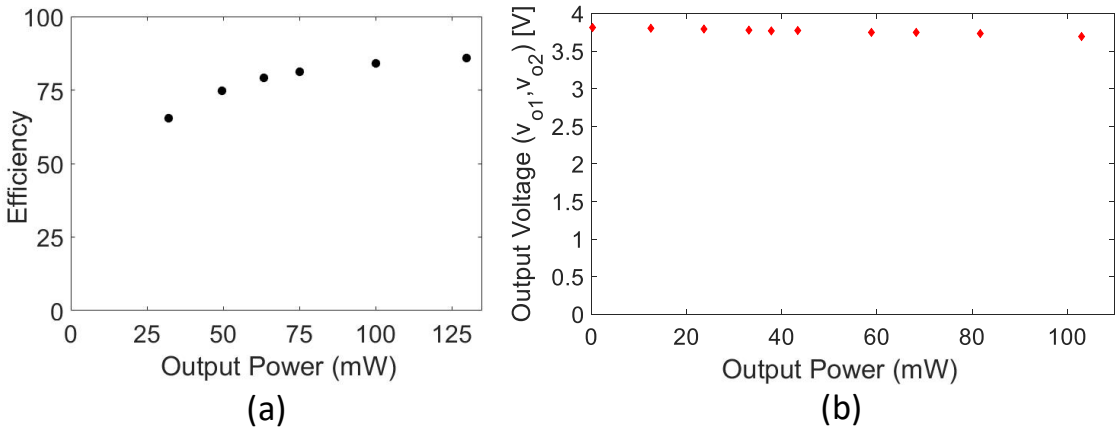

Figure 2.9: (a) System end-to-end efficiency and (b) Converter output voltage w.r.t. output power.

2.5 Conclusion

This chapter introduced a resonant inverter architecture appropriate for wired power transfer between distributed modules of a biomedical implant. The proposed inverter comprises a full-bridge inverter and two T-LCC resonant networks that help generate the required ac output voltage. It is demonstrated that this T-LCC resonant inverter topology can maintain near-constant output voltage across a wide load range without closed-loop control. The proposed inverter can also achieve high efficiency by minimizing circulating losses and maintaining soft-switching across a wide load range. A 130-mW, 1-MHz prototype T-LCC resonant inverter achieves a full power efficiency of 86% and maintains efficiency above 80% across a two-to-one power range. Furthermore, the converter achieved power density of $12W/in^3$.

CHAPTER 3

Leadless and Batteryless Wirelessly Powered Intravenous Cardiac Pacemaker

3.1 Introduction

Over 1 million cardiac pacemakers are implanted worldwide annually in patients suffering from heart block and bradyarrhythmias [16]. Despite a lengthy history of cardiac pacemaker technology, pacemakers continue to suffer from lead-related complications. A traditional lead-based pacemaker is a battery-operated device that is implanted in the chest with the lead that goes from the subclavian vein inside the heart, as shown in Fig. 3.1. Due to the presence of transvenous leads, cardiac pacemakers suffer from short-term and long-term lead-related complications. Short-term complications (within 2 months of pacemaker implantation) can be as high as 8% to 12% and are typically related to to transvenous leads or subcutaneous pocket. These complications include lead dislodgement, pneumothorax, cardiac perforation, and pocket infection or hematoma. Furthermore, long-term complications like a lead fracture,

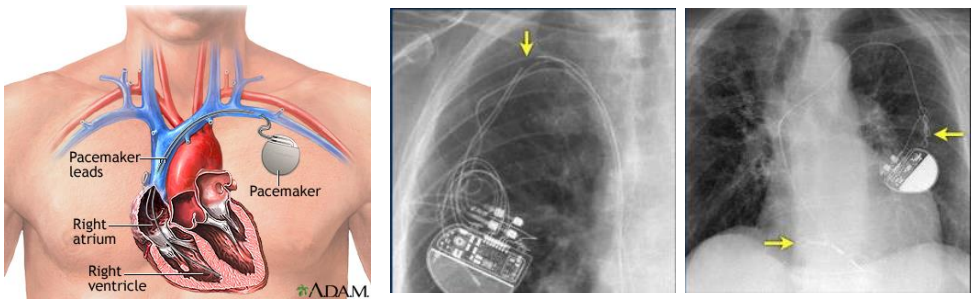

Figure 3.1: (a) Traditional lead-based cardiac pacemaker and lead related complications: (b) Lead breakdown [1], (c) Twiddler's syndrome [1].

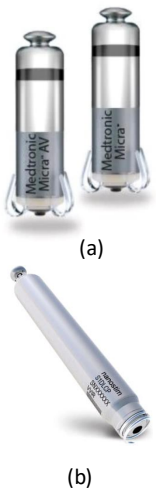

Longevity

Projected service life in years*

VVIR or VVI pacing %	Amplitude	Pacing Rate	Impedance	Longevity in Years	
				Pulse width 0.24 ms	Pulse width 0.4 ms
0%	1.5 V	60 min^{-1}	500 Ω	14.6	14.5
50%	1.0 V	60 min^{-1}	500 Ω	13.3	12.5
	1.5 V	60 min^{-1}	500 Ω	11.7	10.4
	2.0 V	60 min^{-1}	500 Ω	9.6	8.1
100%	1.0 V	60 min^{-1}	500 Ω	11.8	10.5
	1.5 V	60 min^{-1}	500 Ω	9.6	8.0
	2.0 V	60 min^{-1}	500 Ω	7.1	5.5
	2.5 V	60 min^{-1}	500 Ω	5.8	4.3
100%	1.5 V	60 min^{-1}	400 Ω	9.0	7.4
	1.5 V	60 min^{-1}	600 Ω	10.0	8.4
100%	1.5 V	70 min^{-1}	500 Ω	9.1	7.5
	1.5 V	100 min^{-1}	500 Ω	8.0	6.4
100%	2.5 V	60 min^{-1}	600 Ω	6.3	4.7
	3.5 V	60 min^{-1}	500 Ω	3.6	2.4
	5.0 V	60 min^{-1}	500 Ω	1.8	1.2

(c)

Figure 3.2: Modern leadless pacemaker: (a) Medronic Micra pacemaker and (c) ST Jude Nanostim pacemaker. (c) Micra pacemaker datasheet excerpt showing device longevity .

insulation breaks, venous obstruction, tricuspid regurgitation, and Twiddler's syndrome, shown in Fig. 3.1(b,c) can occur which require additional interventions and puts the patient at risk of significant morbidity [17, 18]. Some studies have shown that lead is primarily responsible for long-term complications, identifying it as the weakest component of lead-based pacemakers [18]. Past research on traditional lead-based cardiac pacemakers with low power consumption [2](Fig. 3.3(a)) does not overcome lead-related complications. Wirelessly powered pacemaker proposed in [3, 19] (Fig. 3.3(b)) replaces primary cell with a secondary cell but the need for a lead still introduces lead-related complications.

Modern leadless pacemakers such as Medtronic Micra and ST Jude Nanostim (Fig. 3.2(a,b)) are single-chamber pacemaker devices. They mitigate lead-related complications and have substantially reduced form factor, allowing them to be implanted inside the heart using a catheter. The small form factor imposes battery size constraints. The battery lifetime is 1.2 years (5V @ 0.4ms) to 11.8 years (1V @ 0.24ms) with 100% pacing (Fig. 3.2(c)) and the device needs replacement within the patient's lifetime [20]. Device retrieval can be challenging [18], and, in some cases, the device must be abandoned.

Recently, a leadless and wirelessly powered pulse generator is proposed [4] and shown in Fig. 3.4(a). It has large input power (1W) (1000× higher than the proposed design) which

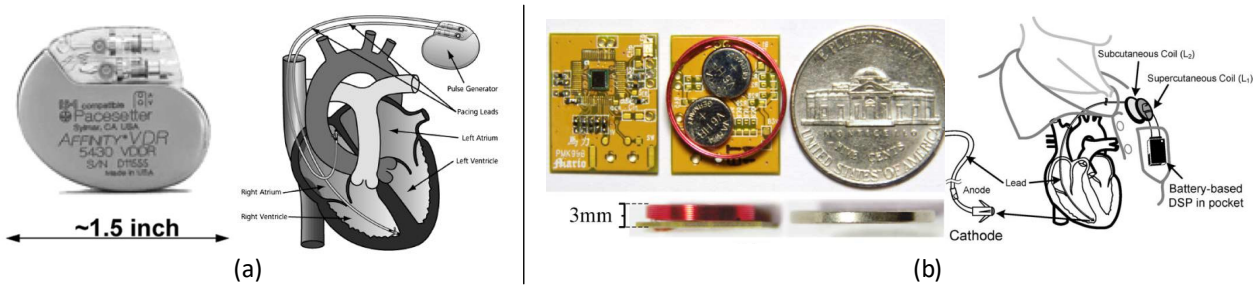

Figure 3.3: A lead-based pacemaker proposed in [2] and a lead-based wirelessly powered pacemaker proposed in [3].

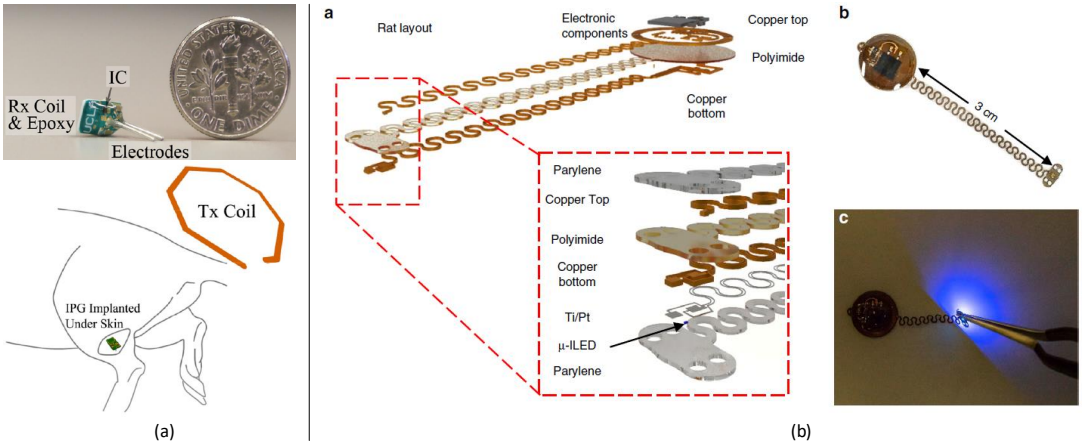

Figure 3.4: A leadless and wirelessly powered pacemaker proposed in [4] and an animal implantable pacemaker proposed in [5].

can deplete the battery quickly and output stimulation voltage is fixed to 3.5V which is lower than the maximum stimulation voltage needed (5V) for a pacemaker to cover broad range of patients [20]. Furthermore, it has post-pulse voltage build-up which can damage the tissue, and stimulation pulse periods are much shorter (∼3x) than the maximum required in pacemakers.

A wirelessly powered and batteryless pacemaker is proposed in [5] and shown in Fig. 3.4(b). The pacemaker is primarily designed to be implanted in an animal with a transmitter coil placed in the animal cage. It is not suitable to be implanted into human subjects.

While the pacemaker technology has significantly matured, lead-related complications continue to be a major limitation in the deployment of the devices. Leadless and battery-based pacemakers have mitigated lead-related complications and have a significantly reduced form factor, but their small form factor also limits the battery size and the device operation

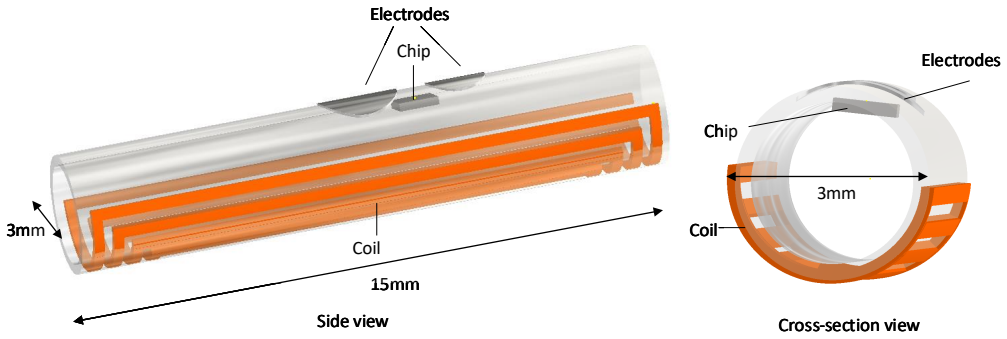

Figure 3.5: Envisioned intravenous cardiac pacemaker (a) side view and (b) cross-section view.

time. Thus, there is a need for a leadless and batteryless pacemaker that mitigates lead-related complications and extends device lifetime. The device can be made leadless by implanting it directly in the heart and batteryless by wirelessly powering the device. Since the device is wirelessly powered, specific absorption rate (SAR) limitation set by FCC must be obeyed. Furthermore, the device must be capable of pacing with similar performance as traditional and leadless pacemakers to be useful practically and have a small form factor to conveniently fit inside the heart.

This chapter presents a leadless, batteryless, and wirelessly powered intravenous cardiac pacemaker that can potentially mitigate lead and battery-related complications of traditional and leadless pacemakers. The pacemaker applies monophasic and cathodic voltage/current stimulation with stimulation characteristics like traditional lead-based and leadless pacemakers. The envisioned intravenous cardiac pacemaker is shown in Fig. 3.5. It is designed to be implanted in a cardiac vein, imposing significant constraints on the form factor. The device is flexible and envisioned to be deployed using a catheter or other minimally invasive approach, easing device implantation and clinical usage.

3.2 System considerations

System considerations are discussed in detail to provide insight of pacemaker functionality and understanding of important considerations in the pacemaker design.

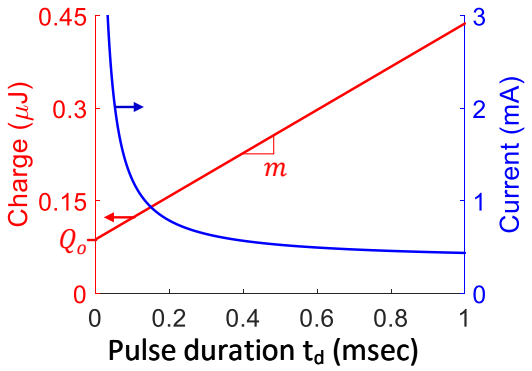

Figure 3.6: Typical strength-duration curve of myocardium.

3.2.1 Strength duration curve

The strength-duration curve is shown in Fig. 3.6 [21, 22]. The curve is based upon the charge-time relationship and determines the minimum amount of charge needed to stimulate the myocardium. It states that the minimum charge needed to stimulate the tissue is directly proportional to the pulse period, as shown in Fig. 3.6. Thus, the relationship can be expressed as:

$$Q = mt_d + Q_o. \tag{3.1}$$

Here, Q is the minimum charge needed to pace the heart for a pulse of period t_d, m is the slope and Q_o is y-intercept. From this expression, the required pacing current amplitude w.r.t. pulse period can be determined:

$$I = \frac{Q_o}{t_d} + m. \tag{3.2}$$

The current amplitude is also plotted in Fig. 3.6. Equation 3.2 establishes the relationship between pacing current amplitude and pulse period and is called the strength-duration curve. Since the electrode-electrolyte interface is primarily resistive [21, 22], a similar strength-duration curve can be derived for voltage amplitude w.r.t. pulse period. Modern electrodes have a similar strength-duration curve for voltage and current stimulation [21].

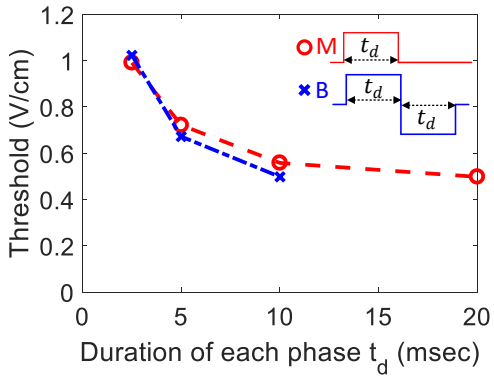

Figure 3.7: Strength-duration curve for monophasic (M) and biphasic (B) stimulation adopted from [6].

3.2.2 Monophasic, cathodic and voltage/current stimulation

Three important aspects of the nature of stimulation must be determined:

- Monophasic or biphasic stimulation,
- Anodic or cathodic stimulation,
- Voltage or current stimulation.

3.2.2.1 Monophasic vs. biphasic stimulation

In [6], it has been shown that if stimulation is applied such that the pulse period of monophasic stimulation equals the pulse period of one phase of biphasic stimulation, the strength-duration curve is similar. The strength-duration curves for monophasic and biphasic stimulation are shown in Fig. 3.7. Thus, adding an extra phase to biphasic stimulation has no significant effect. In fact, monophasic stimulation consumes half the energy to stimulate the tissue with the same voltage threshold as compared to biphasic stimulation, as only one pulse needs to be applied. Monophasic stimulation is therefore preferred for stimulation to extend the battery lifetime by $\sim$2x.

It should be noted that the charge injected during monophasic pulse must be neutralized by shorting the electrodes after stimulation to avoid charge build-up and consequent tissue damage.

3.2.2.2 Anodal vs. cathodal stimulation

The stimulation amplitude required for anodal stimulation is ∼2-3x higher than that for cathodal stimulation [23]. Furthermore, anodal stimulation can result in hyperpolarization of tissue and can generate tachyarrhythmias in the setting of myocardial ischemia or electrolyte imbalances [21, 24]. Thus, anodal stimulation is typically not preferred in cardiac pacemakers. Although in the clinical setting it might be difficult to identify if the pacemaker is doing anodal or cathodal stimulation, electrodes can be designed to prefer cathodal stimulation.

In bipolar-lead pacemakers, as considered here, anodal stimulation is avoided by making the anode with a larger surface area than the cathode. Thus, the higher current density at cathode likely results in cathodal stimulation [21].

3.2.2.3 Voltage vs. current stimulation

Traditionally, pacemakers are designed to stimulate the myocardium with constant voltage pulse [20, 2, 3, 19, 4, 5]. Electrodes that exhibit significant polarization have a chronaxie pulse period for current stimulation much higher than that for voltage stimulation. [23] shows that the chronaxie pulse period is ∼2x higher for current stimulation as compared to voltage stimulation. Correspondingly, the energy required for heart pacing is higher for current stimulation as compared to voltage stimulation. Since traditional pacemakers are designed to last for years, voltage stimulation is the more suitable choice.

Electrodes that exhibit insignificant polarization, which are more commonly used in recent devices, have similar strength-duration curves for both voltage and current stimulation [21, 25]. Furthermore, current stimulation benefits from constant pacing current if the electrode-electrolyte impedance changes over time, for example, due to fibrosis formation. Therefore, either current or voltage stimulation can be used to pace the heart. Our design supports both voltage and current-based stimulation.

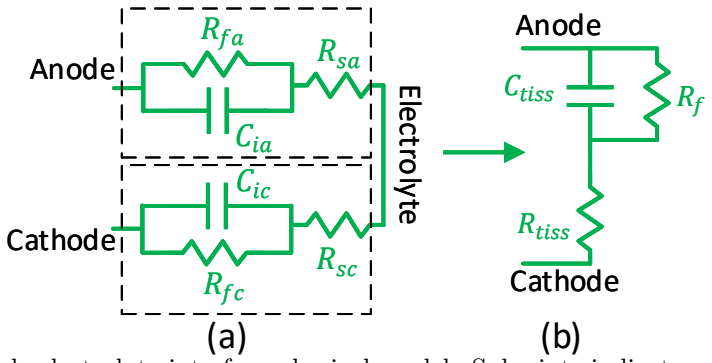

Figure 3.8: (a) Electrode-electrolyte interface physical model. Subscipts indicate anode ("a") and cathode ("c") related parameters. (b) Simplified model.

3.2.2.4 Electrode-electrolyte interface

The interface between an electrode and electrolyte can be modeled with a capacitance, where the electrode forms one plate and ions in the electrolyte from the other plate. When an electrode is inserted in the electrolyte, two layers of charged particles consisting of water molecules and ions are formed in the electrolyte surrounding the electrode which forms a double-layer capacitance and modeled as a capacitor C_i. Furthermore, reduction-oxidation reactions occur between electrode and electrolyte which lead to Faradic charge transfer resistance R_f. Finally, once the charge enters the electrolyte, it incurs the spreading resistance R_s. The full model of electrode-electrolyte for anode and cathode is shown in Fig. 3.8(a) [26, 27]. If the anode surface area is α times large than the cathode, then the model can be simplified as shown in Fig. 3.8(b). Since the double-layer capacitance and Faradiac charge resistance scale with the geometric surface area, the parameters of the simplified model are given as:

$$R_f = R_{fa}(1+\alpha), C_{tiss} = C_{ia}(\frac{1}{1+\alpha}), \tag{3.3}$$

$$R_{tiss} = R_{sa} + R_{sc}. \tag{3.4}$$

It is noted that for voltage and current stimulation, lead impedance R_{tiss} should be maximized by decreasing the surface area of electrodes. Decreasing surface area increases the current density at the electrodes and depolarization of nearby myocytes can be achieved with lower currents. This reduces the energy required for pacing the heart and extends

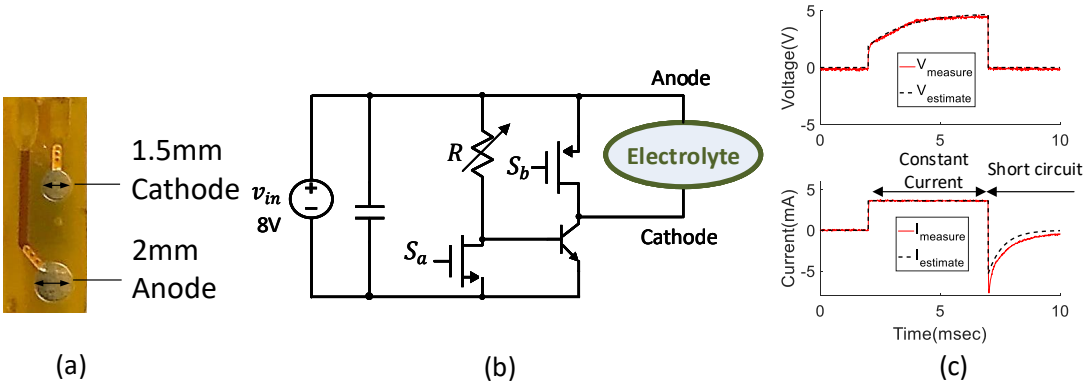

Figure 3.9: (a) Electrodes used in pacemaker and (b) circuit used for electrode characterization.

battery life. But reducing the surface area reduces the tissue capacitance, resulting in higher voltages across the double-layer capacitor (C_{ic}, C_{ia}). If the voltage is too high, it can create non-reversible redox reactions which can permanently damage the electrodes [27]. This can be avoided by either not significantly reducing the electrode surface area or by using porous electrodes, as spreading resistance R_{tiss} depends upon effective surface area, while the double-layer capacitance depends upon actual surface area. Lead impedance R_{tiss} of $500 - 1000\Omega$ is typically used in pacemakers [21, 22].

The gold-plated electrodes used in the pacemaker are shown in Fig. 3.9(a). The cathode is designed to be larger than the anode as discussed previously. The circuit shown in Fig. 3.9(b) was used to characterize the electrodes. A pulse of constant current is applied by a BJT operating in an active region. When the pulse needs to be applied, switch S_a is turned off because of which BJT moves from cut-off to active region. Once the pulse is applied, switch S_a is turned on to cut-off the BJT and switch S_b is turned on to short the electrodes and allow charge neutralization. The amplitude of the current stimulation is controlled by resistor R. The estimated parameters of electrodes from comparison of measurement and model (Fig. 3.9(c)) are: $R_{tiss} = 520\Omega, C_{tiss} = 2\mu F, R_f = 800\Omega$.

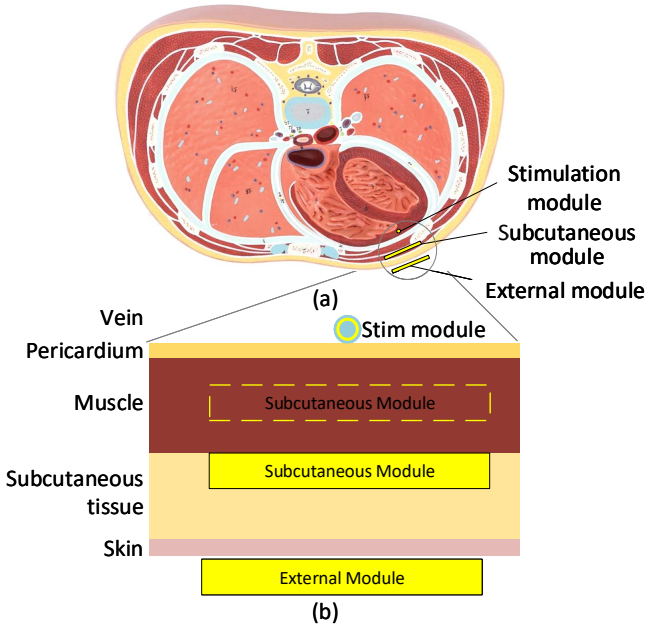

Figure 3.10: (a) Human chest cross-section with implanted modules and (b) zoomed view showing complete system.

3.2.2.5 Device architecture and constraints

A pacemaker is a critical component and cannot be removed by the patient. Thus, the module that transmits wireless power to the pacemaker must be implanted subcutaneously. This leads to a modular architecture comprising of three modules: external module, subcutaneous module, and pacemaker module. Figure 3.10(a) shows the human chest cross-section along with the three modules. The stimulation module is implanted in a vein. Possible veins where the stimulation module can be implanted include greater cardiac vein, anterior interventricular vein, or anterior cardiac vein. The diameter of different veins can vary at different locations. The device diameter is constrained to be 3mm to fit inside the vein (for example greater cardiac vein is ∼3-4mm in diameter [28]). Furthermore, the device thickness must be constrained to allow blood flow in the vein.

The subcutaneous module can either be implanted in the subcutaneous tissue or intramuscularly. Figure 3.10(b) shows the cross-section view from the skin to the greater cardiac vein. The distance between the two from the parasternal area is $32.1 \pm 7.9mm$ and from the apical area is $31.3 \pm 11.3mm$ [29]. If the subcutaneous module is implanted in the subcu-

taneous tissue or intramuscularly, the distance between the subcutaneous and stimulation module is ∼2-2.5 cm. Thus, the device should be designed to operate up to ∼3 cm distance between the subcutaneous module and stimulation module.

The subcutaneous module contains a rechargeable battery that must be recharged from an external module once in few months. Although the distance between the external and subcutaneous module is ∼1cm, the external module can be misaligned from the subcutaneous module. Furthermore, distance variations between the two can occur due to patient movements. To accommodate the variations, the subcutaneous and external modules are designed to have a distance variation of up to 3cm. The circuit used for wireless power transfer between external and subcutaneous modules is presented in Chapter 4. The circuit has an output power of 330mW that can charge a 280mAh Quallion battery QL0280 (3.27cc) [30] in 3 hours. A fully charged battery can last for 1.4 months. The battery has greater than 85% capacity retention after 500 charge/discharge cycles which will allow safe use for more than a decade.

3.2.2.6 Wirelessly powered pacemaker specifications

Based on the discussion in this section, specifications for the pacemaker chip are determined and listed in Table 3.1. Pacemaker should be designed to apply monophasic and cathodic stimulation, where the pulse could have either constant current or constant voltage amplitude. Pulse periods for pacemaker typically varies from 0 to 1msec. Pacemaker electrodes are usually designed to have an impedance of $500 - 1000\Omega$. The stimulation current required for pacing should be programmable from 0 to 5mA to adequately address a range of patient's needs. If voltage stimulation is applied, 5V pacing is needed to cover broad range of patients with different complications [31, 32]. Traditional pacemakers are designed to pace up to 5V with a maximum 1msec pulse width [20]. Therefore, the designed pacemaker must be able to pace up to 5V to be practically useful. Distance between subcutaneous module and stimulation module can vary from 0 to 2.5cm as discussed in Section 3.2.2.5 and the pacemaker should be able to reliably operate within the specified range.

Table 3.1: PACEMAKER SPECIFICATIONS.

Parameter	Value
Stimulation	Monophasic, cathodic and current/voltage
Pulse period	0-1msec
Electrode impedance (R_{tiss})	500-1000 Ω
Stimulation current (I_{out})	0-5mA
Maximum stimulation voltage (V_{max})	5V
Maximum TX-RX distance	0-2.5cm
Frequency (f_s)	13.56MHz
TX coil	Air core, 3cm dia., 6 turns
	L = 2 µH, Q = 135
RX coil	Air core, 1.5cm x 6.4cm, 6 turns
	L = 138nH, Q = 8

The wireless power between the modules must be transferred in the industrial, scientific, and medical (ISM) band to obey FCC regulations and 13.56MHz is an attractive option. Operating at high frequency allows coils with fewer turns to be used while having a high Q factor [33]. This results in lightweight coils and reduces the size of the implant. Therefore, air-core transmitter coils are used. Coil diameter was selected to be 3 cm diameter to conform to the standard implant package. Parameters of TX coil are listed in Table 3.1. Finally, the circuit should be designed to consume low power to avoid the inconvenience of recharging it often.

3.3 Limitations of state-of-the-art

A brief discussion of state-of-the-art pacemakers is discussed in Section 3.1. This section will revisit the limitations of state-of-the-art leadless and batteryless pacemaker proposed in [4]. This will motivate major challenges in the pacemaker design and how they are solved in the

proposed work.

A leadless and batteryless pacemaker proposed in [4], and shown in Fig. 3.4(a), has large input power consumption (1W). The pacemaker is designed to minimize the RX power. But it is important to note that system power consumption is of primary concern and not just RX power. The system consumes 1W input power that can deplete a 1Ah battery in 3.6 hours which makes it extremely inconvenient to use. The system has large input power primarily because it is designed to transmit power at a very high frequency of 430MHz. Operating at higher frequency leads to increased switching losses in transmitter switches $E_{loss} = CV_{DD}^2 f_s$ and increased losses in TX and RX coils. Coils resistance increases at higher frequency ($R_{coil} \propto \sqrt{f}$) which results in increased conduction loss. Furthermore, a matching network is used to design the TX which means that half of the transmitted power is lost in the TX conduction loss. TX design is not discussed in the paper and it is quite possible that an inefficient power amplifier topology further deteriorates the system efficiency. Due to low system efficiency, the TX has to transmit energy continuously so that enough energy can be delivered to the implant to stimulate the myocardium. As a result of transmitting power at high frequency, inefficient system design, and continuous TX operation the system input power consumption is very high. Large input power consumption and high system operating frequency also makes the system incompliant with FCC regulation. SAR evaluation of the system reveals that the maximum value of SAR is 1.645W/kg which is higher than FCC regulations (1.6W/kg) for biomedical implants.

Apart from large input power consumption, the system also suffers from low stimulation voltage (3.5V) and a small pulse period (300μs) which is insufficient to cover a broad range of patients with different heart complications [31, 32]. Commercial pacemakers can stimulate with a voltage of up to 5V or pulse period up to 1msec [20]. The system suffers from low voltage stimulation because rectifier topology used in wireless power receiver that converts AC energy into DC energy has a limited output voltage of < 5V due to oxide breakdown of transistors used which is explained in more detail in Secion 3.4.4. Additionally, pulse periods are limited to avoid non-reversible oxidation-reduction reactions which can permanently damage

the electrodes, as the system does not neutralize the charge after stimulation. Finally, it is noted that the electrodes used in the system do not appear to be useful for practical usage. The protruding electrodes can damage the tissue.

The proposed system can overcome the limitations. To reduce the system power consumption, the proposed system is operated at a much lower frequency (13.56MHz) which reduces the switching loss in TX and conduction loss in TX and RX coil. TX topology is a class-D power amplifier that can ideally achieve 100% efficiency. The TX comprises two switches that are realized using Gallium Nitride (GaN) devices. GaN devices have a much smaller capacitance which results in reduced switching loss. Switching loss in the TX switches is further reduced by using the zero-voltage switching technique. No matching networks are used which could result in lossy TX. Instead, the TX and RX coils are resonated with capacitors to transfer power at maximum efficiency from the coils. Lastly, the system is operated in burst mode as compared to the continuous operation which greatly reduces the system input power. Stimulation pulses have a typical period of 0.5msec and pulse repetition frequency is 1Hz (60 beats/min). This results in the on-period duty cycle of 0.05%. Therefore, if a burst of power is transmitted only for a period the stimulation pulse is applied, it results in 2000× smaller average power as compared to peak system power. As a result, the total system power consumption is 1mW which allows 1.4-month operation using a 280mAh battery. A low system input power also results in a system that complies with FCC regulations.

The proposed system can apply 5V stimulation and programmable pulse width exceeding 1msec. 5V stimulation is achieved by proposing a new rectifier topology. The rectifier topology benefits from the use of high voltage devices which have large drain-source voltage but reduces gate-source voltage which can cause oxide breakdown. Furthermore, the circuit does active charge neutralization to avoid non-reversible oxidation-reduction reactions and long-term damage to the tissue. Charge neutralization is achieved without using a large decoupling external capacitor, which is commonly employed in pacemakers, to further miniaturize the implant.

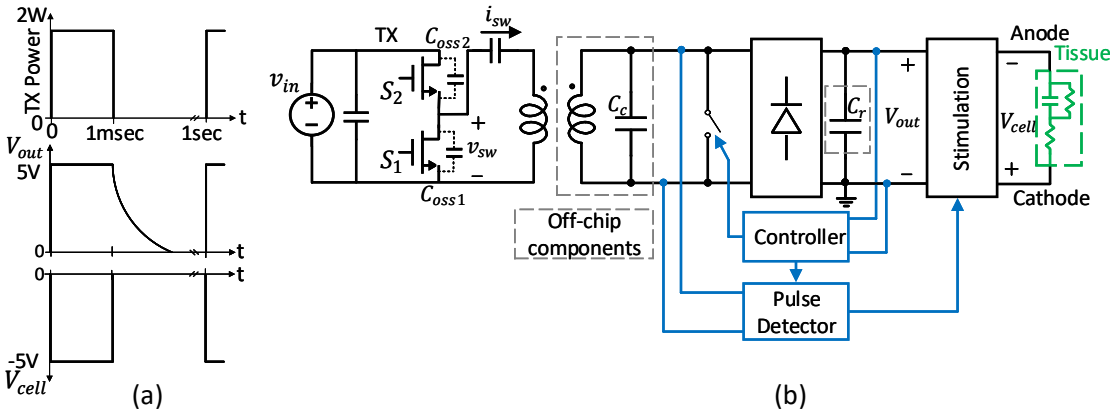

Figure 3.11: (a) TX pulse, RX output voltage, and stimulation pulse, and (b) TX circuit architecture.

3.4 Circuit architecture

Pacemakers operate by stimulating tissue with a pulse of voltage or current. Pulse amplitude and period are defined by the strength-duration curve. Typically, pulse amplitude and period vary from 0.1 to 1 msec and from 0.5 to 5 V, respectively. Pulse frequency dictates human heartbeat and typically ranges from 60 to 100 beats per minute.

To transmit the power wirelessly, TX (subcutaneous module) transmits a short burst of power which is received by RX (stimulation module) and the pulse of the same duration (V_{cell}) is applied to the heart as shown in Fig. 3.11(a). Since the human heartbeat interval (∼1beat/sec) is much longer than the stimulation pulse period (0.1–1msec), TX and RX turn on for a very short time duration (duty cycle: 0.01-0.1%, frequency: ∼1Hz). Therefore, even though when TX is on and it transmits high power (2W), the average dissipated power is much smaller (1mW for 0.5msec pulse), as opposed to an always-on TX which consumes a high average input power (1W) [4]. Furthermore, it allows separation distance between TX and RX to be maximized by transmitting high power in bursts. Lastly, transmitting the power in bursts allows TX to control the frequency and duration of applied stimulation pulses, eliminating the need for an extra data link to control pulse duration.

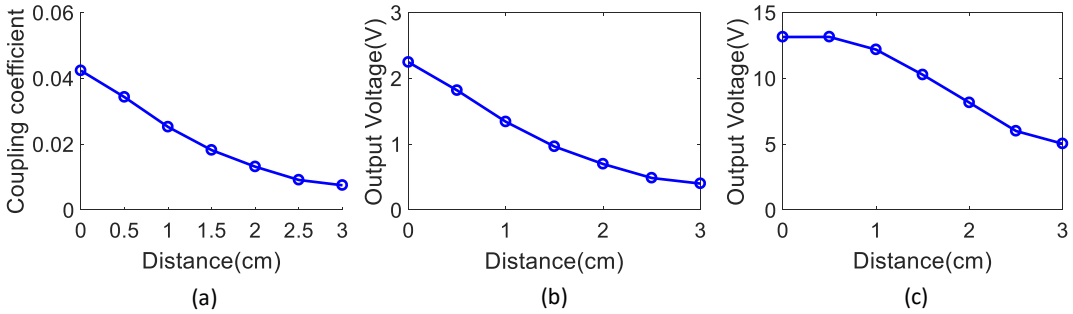

Figure 3.12: Plots of variation w.r.t. distance of (a) coupling coefficient, (b) output voltage of SS WPT system, and (c) output voltage of SP WPT system.

3.4.1 Transmitter (subcutaneous module)

The TX, shown in Fig. 3.11(b) comprises a class-D power amplifier that operates at 13.56MHz ISM band and a 3-cm diameter coil to fit in a standard implant package. The switching loss of the circuit increases with high switching frequency and switch node capacitance. The switching loss is given as: $E_{loss} = C_{sw}V_{in}^2 f_s$, where C_{sw} is the capacitance at switching node and f_s is the switching frequency. If traditional Si devices are used in the half-bridge circuit, the switching loss is substantial due to the devices large parasitic output capacitance $C_{oss1,2}$ which lead to large switch node capacitance ($C_{sw} = C_{oss1} + C_{oss2}$). GaN MOSFETs have significantly reduced output capacitance, allowing them to operate at 13.56MHz with reduced switching loss [34].

3.4.2 Wireless power transfer circuit architecture

The coupling coefficient is used to quantify the coupling between TX and RX coils. The coupling coefficient depends upon the geometry of coils and is given as [35]:

$$k = \frac{k_o}{[1 + 2^{(2/3)}(\frac{d}{\sqrt{r_1 r_2}})]^{(3/2)}}. \tag{3.5}$$

Here, r_1 and r_2 are effective radii of TX and RX coils, d is the distance between the coils and k_o is the maximum coupling coefficient. From the parameters listed in Table 3.1, it can be observed that there is a large asymmetry between TX and RX coils. The coupling coefficient of TX and RX coils is measured in the lab and plotted in Fig. 3.12(a). It can be

noted that the coupling coefficient is very small.

The TX is a voltage mode driver. With a voltage mode driver, the TX coil must be compensated by a series capacitor. RX coil can be compensated by either a series or parallel capacitor which leads to either series-series (SS) or series-parallel (SP) WPT circuit topology [36]. For SS compensated WPT circuit, a ratio of output to the input voltage is given as:

$$\frac{V_{out}}{V_{in}} = \frac{1}{2}\frac{(\omega_o M(\frac{8}{\pi}^2 R_l))}{(R_1(\frac{8}{\pi}^2 R_l) + R_1 R_2 + \omega_o^2 M^2)}. \tag{3.6}$$

Here, R_1 is TX coil resistance, R_2 is RX coil resistant, R_l is the load resistance, ω_o is the operating frequency and M is the mutual inductance which depends on TX and RX coil inductance and coupling coefficient. The output voltage is plotted in Fig. 3.12(b). It can be observed that the output voltage is much smaller than 5V and the topology is not suited for this application.

Similarly, the ratio of output to input voltage for SP compensated WPT circuit can be determined and given as:

$$\frac{V_{out}}{V_{in}} = \frac{2}{\pi}\frac{\omega_o Q_2 M(0.5R_l)}{R_1(0.5R_l) + Q_2^2 R_1 R_2 + \omega_o^2 Q_2^2 M^2}, \tag{3.7}$$

where $Q_l = 0.5\frac{R_l}{\omega_o L_2}$. The output voltage is plotted in Fig. 3.12(c). It can be observed that output voltage is greater than 5V for up to 3cm separation between TX and RX. Therefore, the series-parallel topology is well-suited for pacemaker application.

3.4.3 Receiver (stimulation module)

The RX comprises a coil (6.4mm x 1.5cm) compensated with a capacitor C_c (1nF, 0201), a chip that rectifies AC voltage, and shapes the pulse, a rectification capacitor C_r (100nF, 0201) and electrodes. The circuit architecture is shown in Fig. 3.11(b). When the TX transmits a burst of power, the AC power is received by the receiver. The rectifier rectifies AC voltage and the rectification capacitor C_r charges, which increases the output voltage V_{out} as shown in Fig. 3.11(a). A controller must be present on the RX to regulate the output voltage V_{out}, as the distance between TX and RX is changed. Once the stimulation period

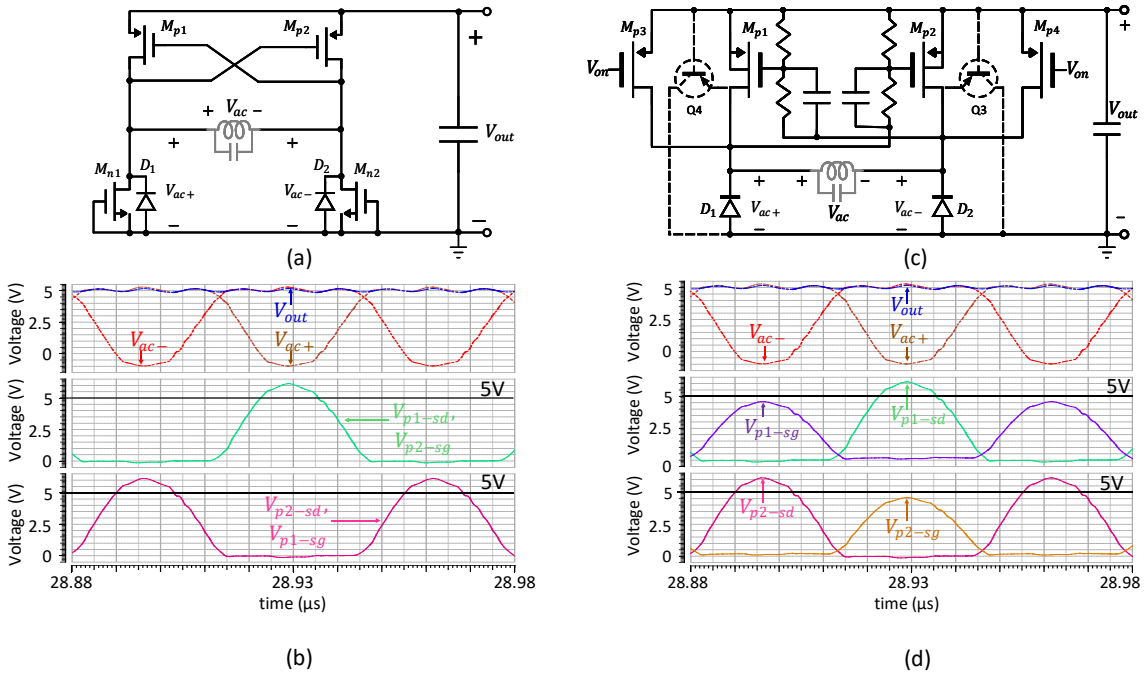

Figure 3.13: (a) Traditional rectifier, and (b) its waveforms. (c) Proposed rectifier, and (d) its waveforms.

is completed, TX stops transmitting power. As a result, the rectification capacitor C_r starts to discharge and V_{out} decreases exponentially as shown in Fig. 3.11(a). If the output pulse is directly applied to the heart, two major issues arise. First, the stimulation period is not well determined as it depends on the discharge time of the rectification capacitor. Second, there is no path for the charge that is deposited in the tissue to neutralize, which will eventually lead to tissue damage.

The two problems are solved by using a pulse detector and stimulation circuit. The pulse detector detects the precise period of TX pulse and informs the stimulation circuit to stimulate tissue for the pulse period. This allows exact control over the stimulation period. Once the pulse is applied, the stimulation circuit shorts the anode and cathode till the next pulse arrives. This provides a path for the injected charge to neutralize and prevents tissue damage.

The circuits used in the chip are described below:

3.4.4 Rectifier

To accommodate patient-specific variations, pacemakers require up to 5V voltage stimulation. Traditional full-bridge rectifier circuits cannot support 5V output voltage due to device breakdown. The rectifier is comprised of PMOS or NMOS cross-coupled transistors connected in series with diode-connected NMOS or PMOS transistors, respectively [3, 19, 37, 36, 38]. A circuit comprised of PMOS cross-coupled transistors in series with diode-connected NMOS transistors (M_{n1}, M_{n2}) is shown in Fig. 3.13(a). Since the structure is comprised of the cross-coupled PMOS transistor, $V_{p1-sg} = V_{p2-sd}$ and $V_{p2-sg} = V_{p1-sd}$. In high-voltage CMOS technology (e.g. 180nm HV BCD Gen2), high-voltage PMOS and NMOS transistors can support high drain-source (V_{ds}) voltage > 50V, but gate-source voltage (V_{gs}) is limited to 5V due to oxide breakdown. Due to the cross-coupled PMOS transistors (M_{p1}, M_{p2}), the source-drain voltage (V_{sd}) is limited by source-gate voltage (V_{sg}) of the devices and no benefit of using high-voltage transistors can be achieved. Figure 3.13(b) shows the circuit waveforms of the rectifier. It can be observed that the cross-coupled PMOS gate-source voltage exceeds 5V during operation if the output voltage is 5V.

It is noted that the root cause of the problem appears because source-gate voltage (V_{sg}) and drain-source voltage (V_{sd}) of cross-coupled transistors (M_{p1}, M_{p2}) is the same. The problem can be eliminated by connecting a potential divider in gate-source voltage as shown in Fig. 3.13(c). The potential divider reduces the gate-source voltage of coupled devices without affecting the drain-source voltage. Furthermore, the potential divider must include a capacitor to compensate for the large gate capacitance of PMOS devices (M_{p1}, M_{p2}). The proposed rectifier waveforms are shown in Fig. 3.13(d). It can be observed from the circuit waveforms that gate-source voltage (V_{p1-sg}, V_{p2-sg}) < 5V, drain-source voltage (V_{p1-sd}, V_{p2-sd}) > 5V and the circuit output voltage is 5V.

In full-bridge rectifier topologies, the AC node voltage (V_{ac+}, V_{ac-}) can go higher than the output voltage (V_{out}) and lower than the ground. If the AC node voltage goes significantly higher than the output voltage (V_{out}), parasitic BJT (Q_3, Q_4) associated with PMOS

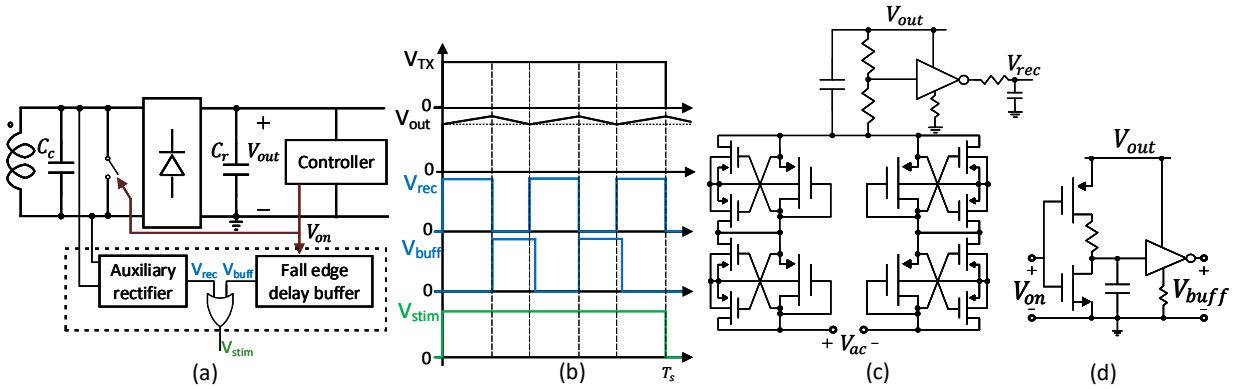

Figure 3.14: (a) Stimulation control circuit and (b) its circuit waveforms. The circuit implementation of (c) auxiliary rectifier and (d) falling edge delay buffer.

transistors (M_{p1}, M_{p2}) can turn on and substantial current will flow in the substrate. To avoid the parasitic BJT turn on, the PMOS transistors are designed to be wide enough to limit maximum voltage drop to 300mV. Furthermore, guard rings are added around PMOS transistors to avoid parasitic BJTs turn on.

Lastly, PMOS transistors (M_{p3}, M_{p4}) acting as switches are added in parallel with PMOS transistors (M_{p1}, M_{p2}), as shown in Fig. 3.13(c), to short the RX coil and allow the rectifier to turn off by the controller.

3.4.5 Controller

The output of the rectifier is regulated by turning on/off the rectifier using a control signal (V_{on}). The controller compares the output voltage of the rectifier (V_{out}) with high and low reference voltages generated from bandgap reference and regulates it between the two thresholds.

3.4.6 Pulse detector

The RX is designed to synchronize its turn on/off with the TX to allow precise stimulation pulse duration control. The RX turns on when TX starts transmitting, but RX turn off could be undetermined due to uncontrolled rectifier capacitor C_r discharging time. To accurately

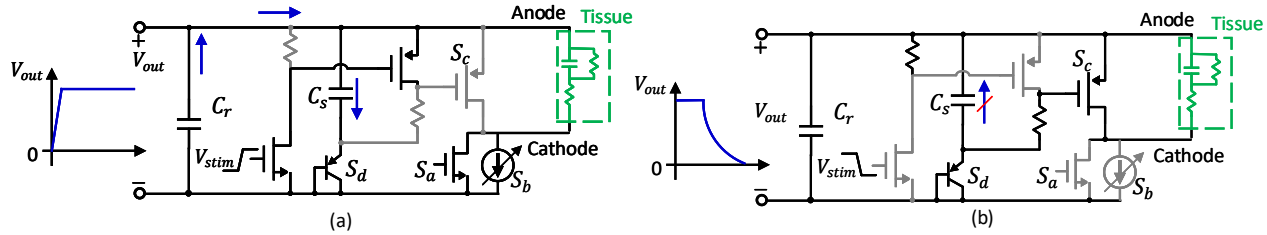

Figure 3.15: Stimulation circuit when pacemaker circuit transitions from (a) passive to active mode and (b) active to passive mode.

detect turn on and off of TX, a pulse detection circuit (Fig. 3.14(a)) employs an auxiliary rectifier to detect the presence of AC signals at the coil outputs. It is noted that when the controller turns off the main rectifier ($V_{on} = 1$), the RX coil is shorted and the auxiliary rectifier senses no AC signal, although the TX is still on. Thus, the output of the auxiliary rectifier is combined using the OR gate with the buffered V_{on} signal (V_{buff}). The falling edge of the control signal (V_{on}) is delayed to create an overlap between V_{buff} and auxiliary rectifier output (V_{rec}). The waveforms illustrating circuit operation are shown in Fig. 3.14(b). It can be observed that combination of auxiliary rectifier and the buffer outputs allow detection of the TX pulse by the RX.

The auxiliary lossy rectifier (Fig. 3.14(c)) is comprised of cascaded diode-connected low-voltage PMOS devices with dynamic body biasing [37] followed by an inverter and a low-pass filter. The auxiliary rectifier uses low-side diodes of the main rectifier. The circuit used for delaying the falling edge of (V_{on}) is shown in Fig. 3.14(d). The pulse detection circuit controls on and off of the stimulation circuit.

3.4.7 Stimulation circuit

Either voltage or current stimulation could be applied to cardiac tissue with similar strength-duration curves [21]. Once the tissue is stimulated, electrodes must be shorted to avoid tissue damage. Traditional pacemaker circuits [2, 3, 19, 4] employ a large series capacitor (∼1-50µF) at the output which ensures no DC flows in the tissue leading to zero residual charge. One extra (large) capacitor is avoided to reduce the RX height and allow the blood to flow through

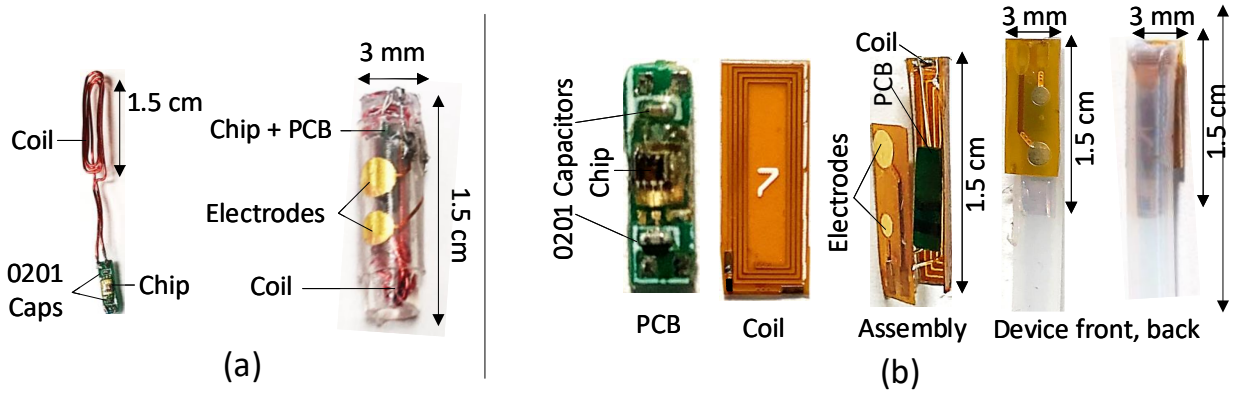

Figure 3.16: Pacemaker components and assembly.

the vein. The stimulation circuit (Fig. 3.15) applies a voltage or current stimulation by turning on the switch S_a or activating the current source S_b, respectively. After stimulation is applied, switch S_c is turned on to short the output (V_{cell}) and ensure zero residual charge in the tissue. When TX turns off, RX also turns off, and the capacitor C_r discharges, which could turn off the switch S_c and prevent electrode shorting after stimulation, damaging the tissue. Switch S_c is kept on after RX turns off by connecting its gate and source terminals to the capacitor C_s. The capacitor C_s in series with the diode S_d is charged when the rectification capacitor C_r is charged by RX turn on, as shown in Fig. 3.15(a), but remains charged even when RX is turned off and C_r is discharged as shown in Fig. 3.15(b). This ensures switch S_c remains on and electrodes are shorted after RX has turned off.

The stimulation circuit can therefore apply voltage or current stimulation pulse for the same period as TX pulse period followed by electrode shorting to neutralize the injected charge.

3.5 Measurement results

3.5.1 System assembly

To test the pacemaker functionality, the chip was wirebonded on a PCB containing a 0201 capacitor, an LED and a resistor as shown in Fig. 3.16. LED and resistor are included

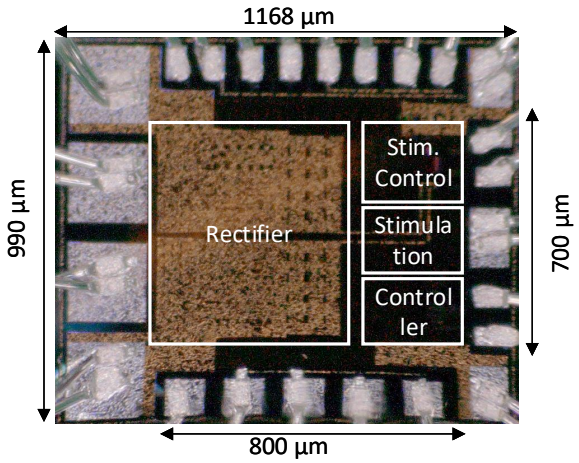

Figure 3.17: Micrograph of the fabricated prototype implemented in 180nm CMOS.

for diagnostic purposes. The PCB was then connected with a coil fabricated on flexible PCB compensated with a 0201 capacitor and gold-plated electrodes. The device was then mounted in a surgical tube and used to test the pacemaker functionality in an animal. The current device assembly is used for chip and device functionality verification. Future work will present detailed system assembly aimed towards chronically implantable leadless pacemakers.

3.5.2 Benchtop results

The intravenous cardiac pacemaker chip was fabricated in a 180nm HV BCD technology, as shown in Fig. 3.17. The chip area is 1.16mm^2 and the total system power consumption is 1mW for a 0.5msec pulse. Figure 3.18(a) shows the TX switched node voltage and current (ref. Fig 3.11(b)). The TX was operated slightly above its resonance frequency to achieve zero-voltage switching (ZVS) of switched devices. From Fig. 14(a) it can be observed ZVS is achieved as the current i_{sw} lags the switch node voltage v_{sw} and the switch node voltage has smooth rise and fall transitions. Figure 3.18(b) shows the AC node voltage (V_{ac+}). It can be observed that the rectifier is operational with >5V peak-to-peak AC voltage. Figure3.18(c,d) illustrates 5mA current stimulation and 5.5V voltage stimulation of the electrode model (R_{tiss}=500 Ω,C_{tiss}=3.3 µF) at a TX-RX distance of 2cm. It can be observed that after stimulation is applied, anode and cathode are shorted together, and cell voltage v_{cell}=0V,

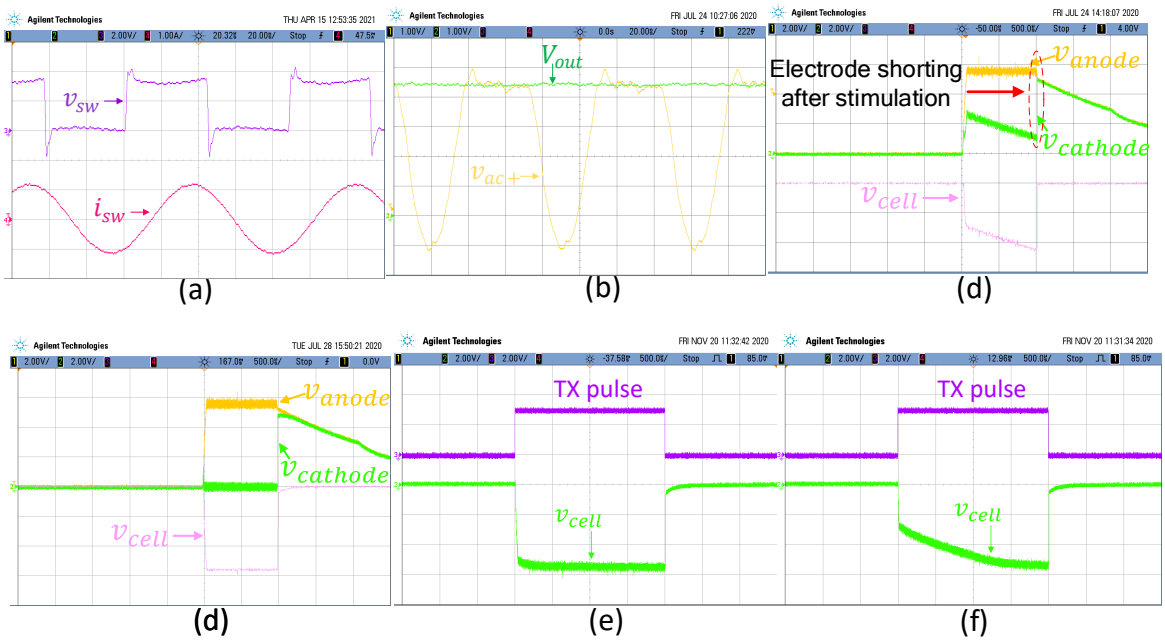

Figure 3.18: Experimental waveforms showing (a) transmitter switched node voltage, (b) rectifier operation, (c) current stimulation pulse, (d) voltage stimulation, (e) synchronization of TX pulse and stimulation pulse for voltage and (f) current stimulation.

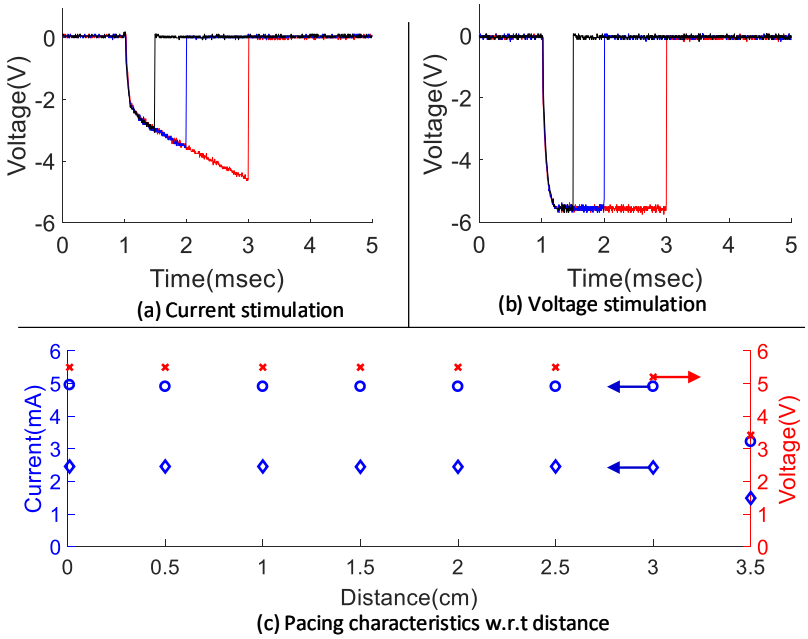

Figure 3.19: Experimental results for varying TX and RX distance of 2cm (a) 2.5mA current stimulation and (b) 5.5V voltage stimulation with pulse duration of 0.5ms, 1ms and 2ms and (c) stimulation amplitude w.r.t. distance.

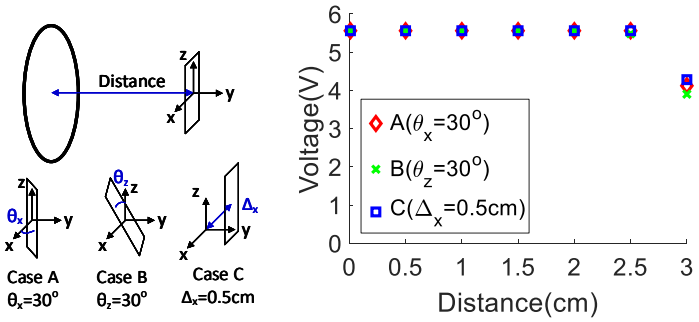

Figure 3.20: (a) Three scanerios depicting RX rotation or misalignment w.r.t. TX and (b) output voltage for the three scanerios.

although the output voltage ($v_{out} = v_{anode}$) decays exponentially. The synchronization of TX and RX pulse periods for voltage and current stimulation is shown in Fig. 3.18(e,f) which demonstrates that the applied pulse period can be accurately controlled from TX. Programmable pulses of 0.5, 1, and 2msec for current and voltage stimulation are shown in Fig. 3.19(a,b). It can be observed that no post-pulse stimulation artifact is present ensuring zero residual net charge in the tissue. The pacing amplitude as the distance between TX and RX is changed is shown in Fig. 3.19(c). The results indicate that the device is operational up to 3cm TX-RX separation, which is sufficient for the implant. Figure 3.20(a) depicts three scenarios in which the RX coil is rotated and misaligned w.r.t to TX coil. The output voltage for the three scenarios is shown in Fig. 3.20(b). It can be observed that under misalignment and rotation between the two coils, the device is operational up to 2.5cm TX-RX separation. Test setup used for bench-top measurement results presented earlier is shown in Fig. 3.21. Components used in subcutaneous and stimulation modules are listed in Table 3.2.

3.5.3 In-vivo results

An in-vivo experiment was performed on a Yorkshire pig to test the functionality of the proposed cardiac pacemaker. The experiment was approved by the UCLA office of animal research. Intramuscular injection of telazol (5mg/kg) was injected into the research animal. The animal was subsequently placed on a ventilator and Isoflurane was given as an anesthetic. Then thoracotomy was performed and a bolus of alpha chloralose was started. Following

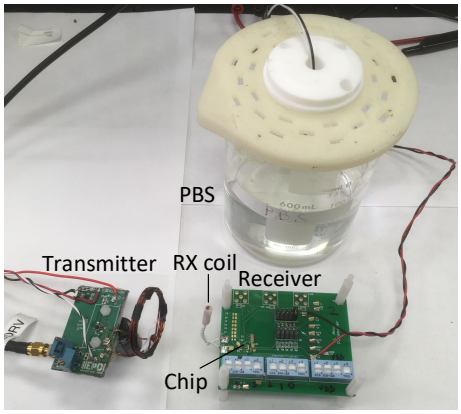

Figure 3.21: Test setup used for bench-top measurement results.

the bolus infusion, Isoflurane was tapered down and the animal was kept on alpha chloralose infusion until the end of the experiment.

Figure 3.22(a,b) shows an in-vivo experimental setup. The proposed pacemaker was fixated in a surgical tube and electrodes were pressed against the pericardium in the right ventricular apex. TX was placed at 2.5cm away from the pacemaker.

Nominal heartbeat was recorded at 64 beats per min (bpm). The transmitter was set to pace the heart at 100bpm with pulse period of 8msec. Significantly longer pulse period was required to pace the heart from pericardium. When the transmitter was turned on, the heartbeat gradually increased to 100bpm in few seconds, and then it decreased back to 64bpm when the transmitter was turned off. ECG signal recording is shown in Fig. 3.22(c) which indicates that heartbeat increased from 64bpm to 100bpm when the pacemaker was turned on and then returned to 64bpm when the pacemaker was turned off.

The animal experiment was performed in an open chest setting. Tissue absorption at 13.56MHz is negligible and penetration depth is >10cm [39]. Therefore, we expect very similar results in a closed chest setting.

3.5.4 SAR evaluation

Long-term exposure to RF waves can be potentially dangerous to humans. Specific absorption rate (SAR) is used to quantify energy absorption due to changing EM fields. Federal

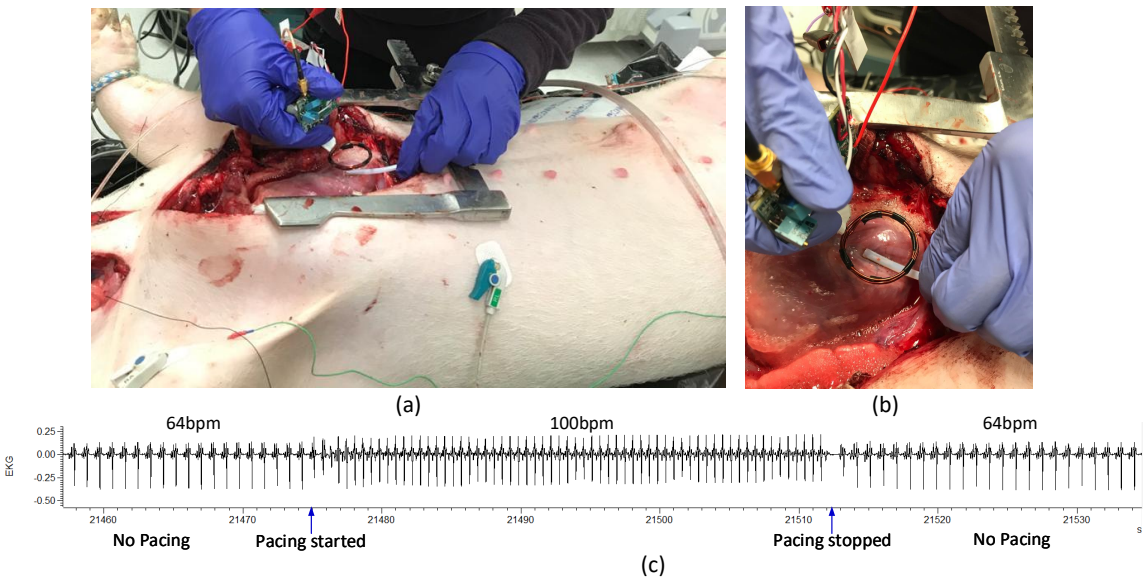

Figure 3.22: (a,b) In-vivo experiment and (c) EKG strip showing increased heart beat.

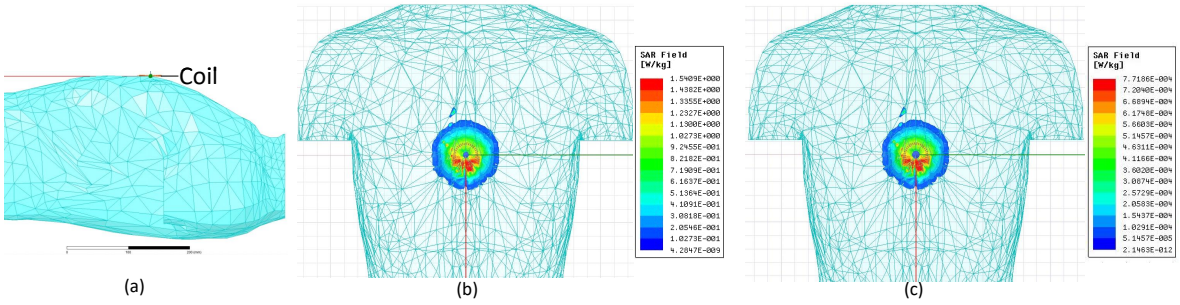

Figure 3.23: (a) Coil location w.r.t. human chest, (b) SAR field plot for max TX power and (c) SAR field plot for average TX power.

Communications Commission (FCC) specifies SAR value to be 1.6W/kg, while IEEE C95.1-2019/Cor 2-2020 specifies 10W/kg for local SAR and 0.4W/kg for whole-body SAR for EM fields in frequency range 3kHz - 300GHz. SAR evaluation of the proposed pacemaker is performed in ANSYS HFSS using the human phantom model as shown in Fig. 3.23. A 3-cm diameter TX coil touching the human chest is stimulated with an average power of 1mW. The SAR field plot is shown in Fig. 3.23. The max SAR field is 1.54mW/kg which is ∼10x lower than FCC regulations (1.6W/kg) and well below IEEE regulations (10W/kg).

3.6 Comparison with state-of-the-art

Comparison of the proposed work with state-of-the-art is presented in Table 3.3. A lead-based pacemaker proposed in [2, 3] is limited by lead-related complications. A leadless and batteryless pacemaker proposed in [4] consumes 1000x higher power than the proposed work. Furthermore, the maximum stimulation voltage of 3.5V and stimulation period of 300 µs is smaller than maximum required for pacemakers (5V, 1ms). Additionally the pacemaker violates FCC limits of 1.6W/kg. The proposed pacemaker advances state-of-the-art by meeting all specifications (Table 3.1) needed for pacing the heart, while significantly reducing the TX power consumption. With a 280mAh rechargeable battery implanted in the subcutaneous module, the pacemaker can last up to 1.4 months. This takes the pacemaker significantly closer to be useful for clinical deployment. Furthermore, the pacemaker design is primarily dictated by implantation needs which would greatly facilitate the device deployment and advance state-of-the-art.

3.7 Conclusion

Traditional lead-based cardiac pacemakers suffer from lead-related complications which include lead fracture, lead dislodgement, and venous obstruction. Modern leadless pacemakers mitigate the complications, but, since they are implanted inside the heart with a small battery, their limited battery lifetime necessities device replacement within the patient's lifetime. In this paper, we presented a leadless and batteryless, wirelessly powered intravenous cardiac pacemaker that mitigates both problems. The pacemaker is a passive wireless power receiver (RX) circuit that receives bursts of power from a transmitter (TX) and stimulates the tissue. The pulse period of the burst is controlled to stimulate the myocardium and the frequency is controlled to regulate the heartbeat. The TX power consumption is significantly reduced by turning it on only for the duration the stimulation is applied. The RX is designed to accurately detect the pulse period of TX and stimulate the heart only for that duration. After stimulation, the RX circuit shorts electrodes to neutralize the injected charge.

The circuit applies monophasic, cathodic, and current/voltage stimulation to the heart with a programmable pulse period. It consumes 1mW power for a 0.5msec stimulation pulse, which qualifies for pacemaker application. 5V voltage stimulation and 5mA current stimulation over 2.5cm TX and RX distance with controllable pulse width and pulse frequency is demonstrated.

The research advances state-of-the-art by mitigating limitations of commercial pacemakers, but two major challenges remain. Firstly, for the device to be practically viable, the device assembly needs to be improved. The device must be assembled such that it is hollow from inside and electronics is contained in the periphery as shown in Fig. 3.5. The device must be pacakged in biocompatible polymer like Parylene and the device implantation lifetime must exceed that of leadless pacemakers. Secondly, device flexibility must be significantly improved to ease device implantation using a catheter or similar minimally invasive approach.

The concept of leadless and wirelessly powered pacemaker can be extended to biventricular pacemakers by deploying two stimulation modules in right and left ventricles. The two stimulation modules can be tuned to receive power at different frequencies. As the TX tank Q factor is high, the circuit bandwidth is small (0.1MHz). Therefore, a few MHz of offset in frequencies can easily minimize interference between the devices.

Table 3.2: COMPONENTS USED IN PACEMAKER.

Component	Parameters
RX Coil (Flexible PCB)	L=138nH, Q=10, 1.5cm x 6.4mm, 4turns
Coil compensation capacitor (C_c)	1nF, 0201
Rectification capacitor (C_r)	0.1 µF, 0201
LED	SML-P11UTT86 250 µm height
Resistor	3 kΩ, 0201
TX coil	L=1.85 µH, Q=135, Diameter = 3cm, 6turns
TX switches $S_{1,2}$	EPC8004
TX switches gate driver	LM5113TME
TX compensation capacitor	75pF

Table 3.3: PERFORMANCE COMPARISON WITH STATE-OF-THE-ART.

	[2] TBioCAS' 19	[3] JSSC' 04	[4] TBioCAS' 11	This work
Technology	$0.18\mu m$	$0.5\mu m$	$0.35\mu m$	$0.18\mu m$ HV
Power transfer	Inductive 13.56MHz	Wired	Inductive 13.56MHz	Inductive 6.78MHz
Total power consumption	1W	8 µW	-	$1mW^{\Delta}$
Max. distance	4.5cm	N/A	-	3cm
Stimulation	Voltage	Voltage	Voltage	Current/voltage
Max. pulse duration*	300 µs	>1ms	>1ms	>1ms
Max. stim. voltage	3.5V	7.5V	3.2V	5.5V
Active charge neutralization	No	Yes	Yes	Yes
Assembly dimensions	$7\times4.1\times1mm^{3\ddagger}$	N/A	$22\times22\times3mmm^{3\dagger}$	$15\times\pi\times2.25mm^3$
Leadless	Yes	No	No	Yes
Batteryless	Yes	No	No	Yes
In-vivo test	Rat leg	No	Rat heart	Porcine heart
FCC SAR limit compliant	No	N/A	-	Yes
External components	Coil + LED + 3-0603 caps	Discrete	Coil + lead + 2-batteries + caps	Coil + 2-0201 caps

∗Required pulse duration: 0-1msec

†Excluding lead and encapsulation

‡Excluding electrodes and encapsulation

ΔOutput power for 0.5msec output pulse

CHAPTER 4

A Burst-Mode Controlled Inductive Wireless Power Transfer System

Research in wireless power transfer (WPT) has seen prominent growth over the past few years [40]. Our understanding of wireless power transfer has increased over the last decade and technologies employing WPT are becoming more widespread. Wireless power transfer has found applications in consumer appliances including phone and tablet chargers, electric vehicle chargers, and biomedical implants, and the applications are growing with time.

Wireless power transfer for biomedical implants presents unique challenges. A patient can have movement while wearing an external charger that is charging the implant. Additionally, it can be difficult to align the external charger with the implant. Magnetic alignment of external transmitter and implant is sometimes used, which is inconvenient to the user. Thus, it is desired for biomedical implants that the WPT system has immunity to reasonable distance variations. Furthermore, implant power consumption can change with patient needs. Therefore, the WPT system should be designed to regulate system output voltage against load variations. Finally, the WPT system should achieve high power transfer efficiency and

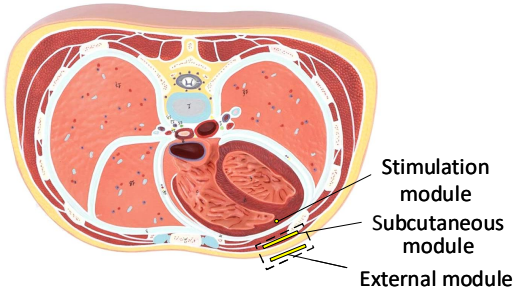

Figure 4.1: Chest cross-section showing the WPT system placement.

Table 4.1: DESIGN SPECIFICATIONS OF WPT SYSTEM.

Parameter	Value
Input voltage (V_{dc})	6.5V
Output voltage (v_{out})	5V
Output power (P_{out})	0-330mW
Frequency (f_s)	6.78MHz
TX coil	3cm diameter, 6 turn
RX coil	3cm diameter, 6 turn
Maximum distance	3cm

both transmitter and receiver should be lightweight and small enough to fit in a standard implant package. The application considered in this paper is a cardiac pacemaker shown in Fig. 4.1. The system consists of an external module, an implanted subcutaneous module, and a stimulation module. The focus of this thesis is WPT between external and subcutaneous modules. The power transfer between subcutaneous and stimulation modules happens at 13.56MHz. To mitigate the possibility of unintended excitation of stimulation module from the external module, a frequency of 6.78MHz is selected for WPT between external and subcutaneous modules. System specifications are listed in Table 4.1.

To achieve immunity to distance and load variation, different techniques are employed. In [41, 42, 43, 44] a separate communication link is present between the transmitter (TX) and receiver (RX) as shown in Fig. 4.2(a). An always active backchannel between TX and RX is undesired in biomedical implants. It needs a separate pair of coils and extra resources of RX. Furthermore, the backchannel circuitry on RX can be power-hungry. A separate communication link is avoided in [45] by using an extra sensing TX coil to detect LSK signal. An extra TX coil increases the TX coil area by 86% [46]. Furthermore, the system achieves a very limited operational range of 7mm for 30mW output power which is unsuitable for the considered application. To avoid the extra TX coil, a WPT circuit has been proposed recently [46]. It employs a current sensor on the TX that detects the

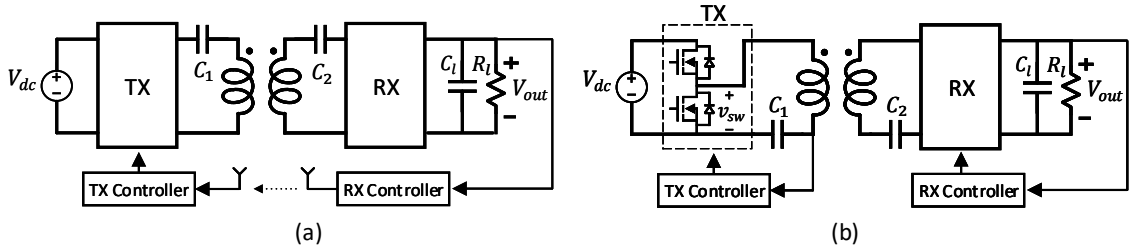

Figure 4.2: (a) A traditional series-series compensated inductive WPT system with TX and RX data link and (b) proposed WPT system.

current amplitude variation in response to load modulation that occurs due to the hysteresis controller employed on the RX. Absolute variation in TX current amplitude sensed output is usually much smaller than absolute variation in TX tank quality factor, as employed in this paper. It is therefore expected that the range of the system would be limited. No range measurements are presented in the paper which make comparisons difficult. Furthermore, reliable current sensing is challenging. Sensing current at the switching node can potentially introduce switching noise coupling in the sensed output. On the other hand, as proposed in this paper, sensing quality factor of TX tank can be easily achieved by sensing voltage across the tank resonant capacitor. Some researchers [47] have proposed that the backchannel link can be avoided by employing a dc-dc converter on the receiver to regulate output voltage against distance and load variations. The presence of a separate dc-dc converter on the RX decreases end-to-end system efficiency and adds more complexity to the circuit. Additionally, in the circuit, the rectified voltage of the RX diode bridge varies with the distance between TX and RX. This can lead to low rectifier efficiency when rectified voltage is small as explained in Section 4.1. The frequency control method for regulating system output for biomedical implants is proposed in [48]. Additionally, a free-running oscillator that changes the oscillation frequency to regulate output voltage without using any extra communication feedback between TX and RX has been proposed in [49, 50]. Changing the frequency of oscillation is undesired if the power transfer happens in ISM bands. Furthermore, the system output power is limited to 100mW if the system remains within the ISM band [50]. The power level is not sufficient for many applications.

In this chapter, we present a burst-mode controlled inductive WPT system with no back channel between TX and RX, as shown in Fig. 4.2(b). Power is transmitted in bursts between TX and RX and the burst period is controlled through load modulation to regulate the system output voltage. Load modulation on RX is detected on the TX by detecting the tank quality factor (Q) and correspondingly the TX is turned on and off. This paper discusses a linear circuit model of the WPT system capturing key loss mechanisms in the WPT system. The model is then used to explain the effect of load modulation. A control circuit used to make the WPT system immune to distance and load variations is introduced. Finally, a 330mW prototype is built to validate the system performance.

4.1 Simplified circuit model of series-series compensated inductive WPT system

A series-series compensated inductive WPT system is shown in Fig. 4.2(b). The WPT system comprises a TX to convert dc power from source to ac power and transmits it over the compensated coils. The ac power is received by the RX compensated coil followed by a diode full-bridge rectifier which rectifies it and supplies power to the load.

An equivalent representation of the circuit is shown in Fig. 4.3(a). Since the circuit is comprised of two high-Q tanks (L_1, C_1 and L_2, C_2), the square-wave voltage generated by the half-bridge inverter from the dc supply V_{dc} can be approximated by a sinusoidal voltage source V_s, as Q factor of both TX and RX tanks is very high and the circuit primarily responds to the fundamental frequency. Similarly, using fundamental frequency approximation, the receiver comprising of the load R_l and diode bridge can be approximated by resistor R_e [51] and a voltage source v_d. The equivalent input voltage source and resistor expressions are given as:

$$V_s = \frac{2}{\pi} V_{dc}, R_e = \frac{8}{\pi^2} R_l. \tag{4.1}$$

Here V_{sw1} is the amplitude of the fundamental component of the half-bridge switched node voltage v_{sw} shown in Fig. 4.2(b). R_1 in Fig. 4.3(a) represents TX resistance comprising of

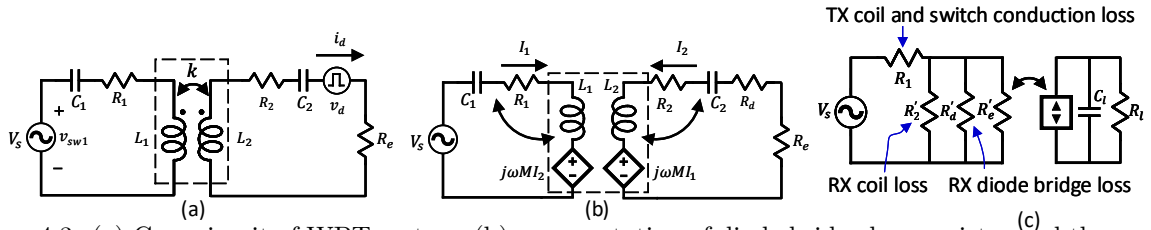

Figure 4.3: (a) Core circuit of WPT system, (b) representation of diode bridge by a resistor and the coupled coils by dependent voltage sources and inductors and (c) simplified and accurate WPT circuit model modeling key loss mechanisms.

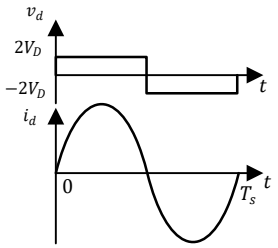

Figure 4.4: Voltage drop and current flow through diode bridge.

switch on-resistance and TX coil resistance and R_2 represents RX coil resistance. The voltage drop v_d and current i_d through the diode bridge is shown in Fig. 4.4. Since the current flowing through the rectifier bridge and equivalent voltage source v_d are predominantly sinusoidal and the power loss only occurs at the fundamental component, the diode bridge can be represented by a resistor. The resistance and the diode bridge efficiency are given as:

$$R_d = \frac{8}{\pi^2} R_l \left(\frac{2V_D}{V_{out}}\right), \eta_d = \frac{\frac{V_{out}}{2V_D}}{1 + \frac{V_{out}}{2V_D}}. \tag{4.2}$$

Here V_{out}, V_D and η_d represent output voltage, diode-on drop voltage, and diode bridge efficiency, respectively. It is noted that the diode bridge efficiency depends upon the ratio of output voltage and diode on-drop voltage ($\frac{V_{out}}{2V_D}$). In WPT circuits with RX comprising of diode bridge followed by dc-dc converter [47] output voltage of the rectifier significantly drops at larger distances. This introduces significant losses in the diode bridge as TX and RX are separated. The proposed circuit, as shown later, regulates the diode bridge output voltage to the intended value and thus achieves fixed diode bridge efficiency for its entire range.

The coupled coils in the circuit can be replaced by an equivalent model consisting of two self-inductances (L_1, L_2) and two dependent voltage sources, as shown in Fig. 4.3(b).

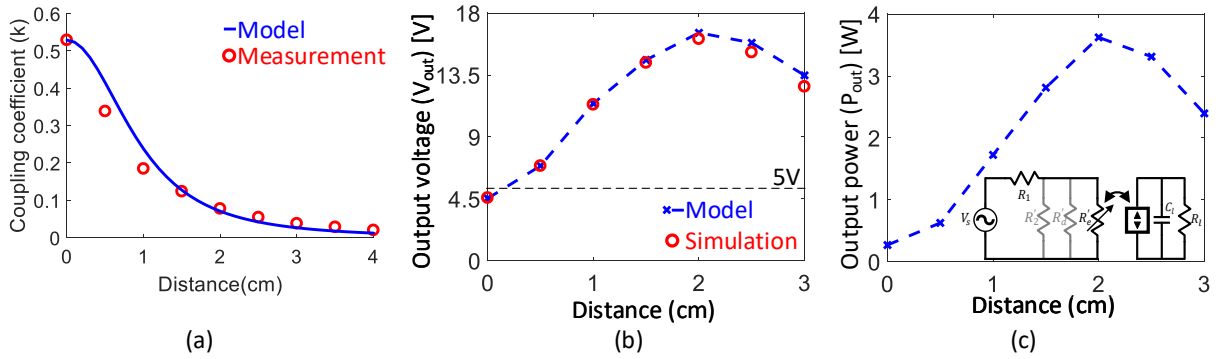

Figure 4.5: Coupling coefficient w.r.t. distance, (b) modeled and simulated output voltage and (c) output power of the circuit w.r.t. distance for a fixed load ($R_l = 76\Omega$).

The coupling coefficient k is captured by two current-dependent voltage sources. The compensating capacitors (C_1, C_2) are designed to resonate with the self-inductances (L_1, L_2), respectively. The circuit can be simplified further by removing the resonant components (L_1, C_1, L_2, C_2), and representing the dependent sources and the resistances R_2, R_d and R_e by their Thevenin equivalent, as shown in Fig. 4.3(c). Here, the equivalent resistances are given as:

$$R_2' = \frac{\omega_o^2 M^2}{R_2}, R_d' = \frac{\omega_o^2 M^2}{R_d}, R_e' = \frac{\omega_o^2 M^2}{R_e}. \tag{4.3}$$

Power delivered to R_e' is delivered to the load R_l, while R_1, R_2' and R_d' represent power loss in the TX coil and TX switches resistance, RX coil, and the diode bridge, respectively. This model captures key loss mechanisms in a WPT circuit: conduction loss in TX switches and coil, RX coil conduction loss, and RX diode bridge loss. The model can be used for predicting circuit losses and output voltage if the coupling coefficient can be determined.

The coupling coefficient characterizes the strength of coupling between TX and RX coils, and it depends upon the geometry of coils. For circular coils of radii r_1 and r_2, the coupling coefficient is adopted from [52] with modified maximum coupling coefficient:

$$k = \frac{k_o}{[1 + 2^{(2/3)}(\frac{d}{\sqrt{r_1 r_2}})]^{(3/2)}}. \tag{4.4}$$

Here, k_o is the maximum coupling coefficient when the distance between the two coils is 0cm. From the experiments, it is noted that the maximum coupling coefficient is less than

1 ($k_o \sim 0.5 - 0.8$). The coupling coefficient of the coil parameters listed in Table 4.1 is experimentally determined. The coupling coefficient measurement result and its comparison with the model is plotted in Fig. 4.5(a). Coupling coefficient can be used to predict the circuit output voltage for a given load R_l using the model discussed earlier, which is given as:

$$\frac{V_{out}}{V_{dc}} = \frac{1}{2}\frac{\omega_o M R_e}{R_1 R_e + R_1 R_2 + \omega_o^2 M^2}. \tag{4.5}$$

The output voltage of the circuit w.r.t distance is plotted in Fig. 4.5(b) and compared with the HSPICE circuit simulation of the WPT system which includes all circuit parasitics. It can be observed that the model matches well with the simulation and the model predicts output voltage reasonably accurately. It is noted that the RX rectifier diodes parasitics capacitance has a negligible effect on the model predictions if the diodes with small parasitic capacitance are selected. The system output voltage is low at a small TX-RX distance, it increases with the distance and finally decreases. The reason is that, as the distance between TX and RX is increased, the reflected load resistance (R'_e) monotonically decreases. R'_e is given as:

$$R'_e = k^2 \frac{\omega_o^2 L_1 L_2 \pi^2}{8 R_l}. \tag{4.6}$$

The term in parenthesis is constant and R'_e decreases as k decreases. As can be observed from the model of Fig. 4.3(c) which is also shown in Fig. 4.5(c), the power delivered to the resistance increases until maximum power point is reached when $R'_e \approx R_1$ after which the power delivered to it decreases. The power delivered to R'_e is shown in Fig. 4.5(c). Since the power delivered to R'_e is delivered to the load, therefore, the output voltage increases and then decreases. It can be observed the system output power is unregulated as the load resistance R_l is fixed for all TX-RX distances. Regulation of the circuit output power can be achieved by modulating the resistance seen by the WPT circuit.

Load resistance seen by the WPT system can be modulated by a circuit shown in Fig. 4.6. Since RX is comprised of a high Q factor circuit with a series inductor, it can be represented by a sinusoidal current source. The current source rectified by the diode bridge rectifier is

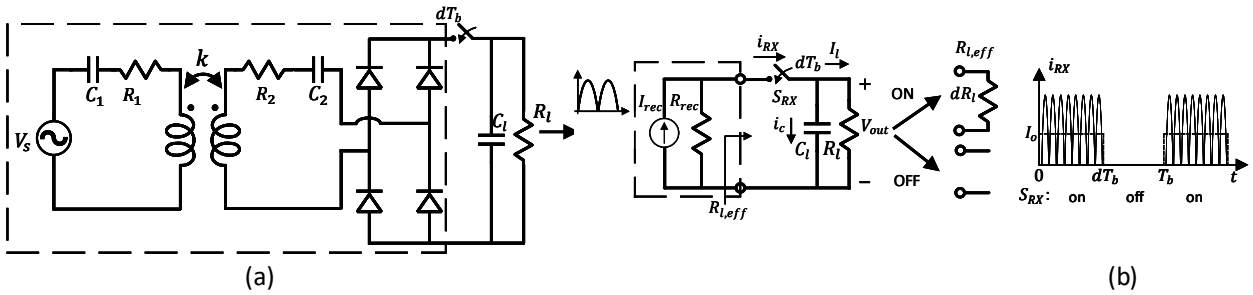

Figure 4.6: (a) Load modulation effective resistance when the switch S_{RX} is on and off and (b) the switch current.

represented by I_{rec}. R_{rec} represents the Norton equivalent resistance. When the switch S_{RX} turns on, the rectified current charges the output capacitor C_l and provides power to the load and when the switch S_{RX} turns off, the output capacitor C_l discharges into the load R_l. The effective resistance seen by the WPT circuit when the switch S_{RX} is on can be determined from the circuit and waveform shown in Fig. 6(a,b) respectively. If the capacitor C_l is large, the output voltage V_{out} across it remains almost constant. Furthermore, no dc current can flow in the capacitor C_l in steady state $\langle i_c \rangle = 0$ Therefore:

$$\langle i_{RX} \rangle = dI_o = I_l. \tag{4.7}$$

Here, I_o is the average value of current that flows through the switch S_{RX} when it is on. Therefore, when the switch S_{RX} is on, the resistance seen by the WPT circuit is given as:

$$R_{l,eff} = \frac{V_{out}}{I_o} = d\frac{V_{out}}{I_l} = dR_l. \tag{4.8}$$

If the switch is periodically turned on and off with a duty cycle d at a frequency much lower than ω_o, the resistance seen by the input is given as:

$$R_{l,eff} = dR_l \quad when\ S_{RX}\ is\ closed, \qquad R_{l,eff} = \infty \quad when\ S_{RX}\ is\ open. \tag{4.9}$$

Thus, by modulating the switch duty cycle, the effective resistance seen by the WPT circuit can be varied. Finally, it is noted that in the burst-mode controlled circuit, the TX turns on when the RX switch S_{RX} is on and it turns off when the RX switch S_{RX} is turned off. Therefore, the effective load resistance seen by the WPT circuit when it is on is dR_l.

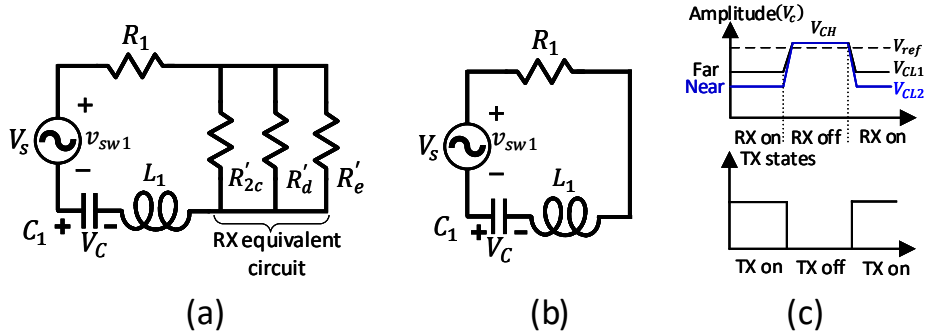

Figure 4.7: Equivalent circuits from TX side when RX switch S_{RX} is (a) on and (b) off. (c) Amplitude variation of rectified capacitor C_1 voltage for different TX-RX distances when the RX turns on and off and (d) corresponding TX states.

4.2 Effect of load modulation

Turn on and off of the receiver switch S_{RX} (load modulation) can be detected by the TX. The model of Fig. 4.3(c) can be used to explain the effect of load modulation on TX. The effective resistance before the diode bridge is given as:

$$R_e = (\frac{8}{\pi^2})R_{l,eff}. \tag{4.10}$$

Therefore, effective diode bridge resistance when the RX switch is on and off is given as:

$$R_{e,on} = (\frac{8}{\pi^2})dR_l \quad and \quad R_{e,off} = \infty. \tag{4.11}$$

The corresponding two equivalent circuits are shown in Fig. 4.7(a, b). TX inductor L_1 and capacitor C_1 are restored in the circuit model, as a voltage across the TX capacitor C_1 is of interest for detecting load modulation. It is noted that when the load is open circuit ($R_e = \infty$), it appears as a short circuit on the primary side as given by Eq. 4.3. From Fig. 4.7(a, b), it can be observed that when RX transitions from on to off state or vice versa, the quality factor (Q) of the tank changes. The Q factors of the tank when RX is on and off can be expressed as:

$$Q_{1,on} = \frac{\omega_o L_1}{R_1 + R'_2||R'_d||R_e} \quad and \quad Q_{1,off} = \frac{\omega_o L_1}{R_1}. \tag{4.12}$$

The quality factors are plotted in Fig. 4.8 w.r.t. distance. The difference between the two Q factors is significant when the TX-RX distance is small and reduces at larger TX-

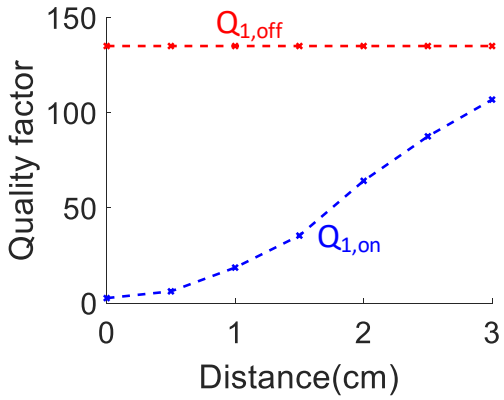

Figure 4.8: Change in TX quality factor w.r.t. distance.

RX distances as can be seen in Fig. 4.8. This implies that the TX can easily detect RX turn on/off when the two are close to each other and detection becomes difficult at larger distances.

To detect the circuit quality factor, the amplitude of the voltage across the capacitor C_1 can be measured. The capacitor voltage can be expressed as:

$$V_c = Q_1 V_{sw1}. \tag{4.13}$$

The amplitude of the voltage across the capacitor C_1 when RX is on and off is plotted in Fig. 4.7(c). If a reference voltage V_{ref} is present between the two voltage levels, TX can determine whether RX is on or off and can correspondingly turn itself on and off as shown in Fig. 4.7(d). This is the underlying mechanism that allows the TX to detect on/off of RX without employing a backchannel data link between the two.

Lastly, it can be noted that when RX is off (Fig. 4.7(b)), the tank Q factor ($Q_{1,off}$) is not dependent on load R_2 or coupling coefficient k and it is constant regardless of distance and load as shown in Fig. 4.8. Therefore, the capacitor voltage C_1 amplitude when RX is off (V_{CH}) is constant irrespective of TX-RX distance and load. On the other hand, when RX is on, the tank Q factor ($Q_{1,on}$) does depend on load and coupling coefficient and correspondingly the capacitor C_1 voltage amplitude when RX is off (V_{CL}) changes with load and distance variations. This is shown in Fig. 4.7(c) for near and far TX-RX distance. Thus, if a reference

voltage (V_{ref}) on TX side is set such that:

$$V_{ref} \leq V_{CH}. \tag{4.14}$$

it can distinguish whether RX is on or off. Furthermore, if V_{ref} is set very close to V_{CH}, a constant reference voltage V_{ref} can be used to distinguish the RX states on the TX side regardless of TX-RX distance and load variations. This allows the controller on TX to be greatly simplified.

4.3 Circuit operation

The circuit architecture employed is shown in Fig. 4.9(a). A burst of power is transmitted from TX at a constant frequency ($f_b = \frac{1}{T_b}$) and duty cycle of the burst is controlled to regulate output voltage against variations in distance and load. Example waveforms of TX on/off and output voltage are shown in Fig. 4.9(b, c). It is noted that when TX is on, it is transmitting at the tank resonant frequency f_o and $f_o >> f_b$.

TX turns on with a constant period T_b. The TX turn on transmits power, which charges the output capacitor C_l. When the output voltage reaches a high threshold (V_H), the RX controller turns off the switch S_{RX}. The switch turns off is detected on the TX side by detecting the capacitor C_1 voltage amplitude V_c. When the capacitor voltage amplitude rises, the TX is turned off at dT_b. The TX remains off for the rest of the duration and turns

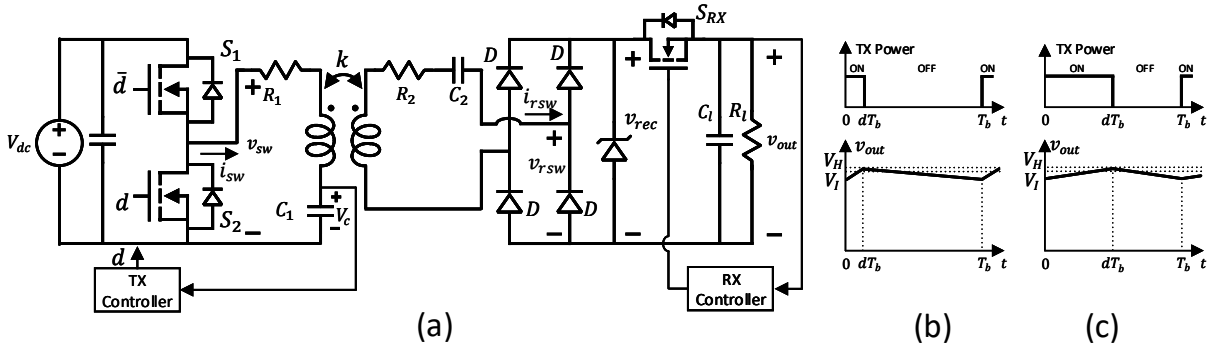

Figure 4.9: (a) Circuit architecture of WPT system and (b, c) circuit output waveforms as the TX-RX distance changes.

on after the period T_b is complete.

When the distance between TX and RX changes, the duty cycle of the burst automatically changes to regulate the output voltage. Two example scenarios with different TX and RX distances are shown in Fig. 4.9(b, c). When the TX and RX distance is changed, the TX turn-on time is automatically adjusted by the controller. Duty cycle modulation of the burst is achieved using load modulation on the RX as explained earlier.

4.4 Control circuits

4.4.1 RX control circuit

To regulate the circuit output voltage, a simple bang-bang controller is designed. The controller turns the switch S_{RX} off when the output voltage V_{out} goes higher than V_H and turns the switch on when output voltage goes lower than V_I, as shown in Fig. 4.9(b, c). It is noted that V_I is higher than the lowest output voltage V_L to ensure that when the TX turns on in the next cycle, switch S_{RX} is on and RX can receive power ($V_H < V_I < V_L$). Furthermore, the output capacitor C_l should be large enough such that output voltage does not go below V_L, which is achieved by choosing an appropriately large capacitance:

$$C_l > \frac{\langle V_{out} \rangle T_b}{R_{l-min}(V_H - V_L)}. \tag{4.15}$$

The receiver controller circuit is shown in Fig. 4.10. The receiver employs a high-side

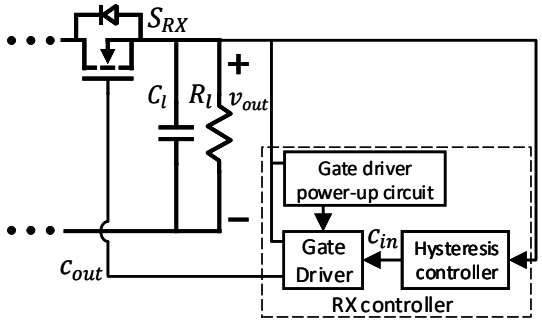

Figure 4.10: RX controller circuit.

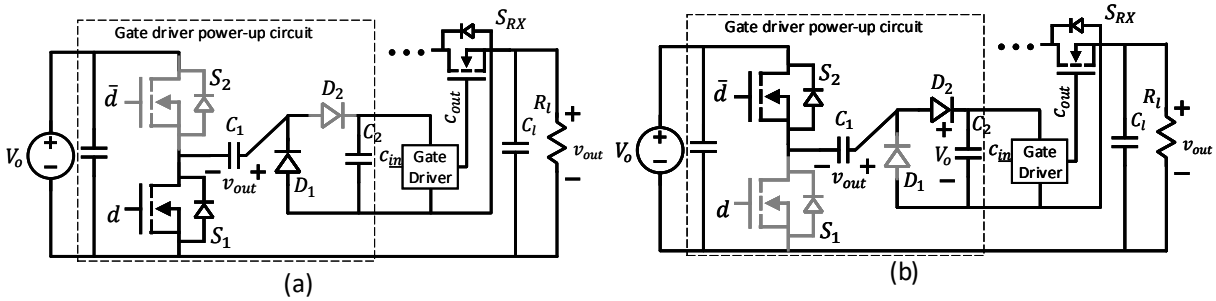

Figure 4.11: (a) Gate driver power-up circuit phase 1 (ϕ_1) and (c) phase 2 (ϕ_2).

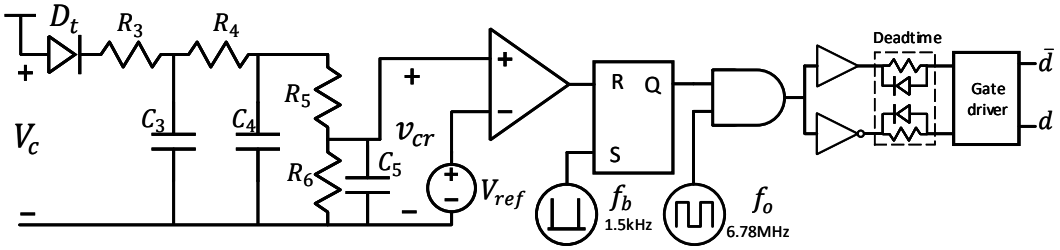

Figure 4.12: Control circuit employed on TX side to detect load modulation.

switch which needs to be periodically turned on and off at a frequency f_b. The standard bootstrap circuit cannot be used to power up the gate drive circuit as the output voltage is not switched. The circuit employed to power up the high-side gate driver is shown in Fig. 4.10(a, b). A half-bridge circuit (low-side gate driver) comprising of switch S_1 and S_2 is used to generate the supply voltage for the gate driver (high-side gate driver). In phase 1 (ϕ_1) shown in Fig. 4.10(a), switch S_1 and diode D_1 turn on to charge capacitor C_1 with v_{out}. In phase 2 (ϕ_2) shown in Fig. 4.10(b), switch S_2 and diode D_2 turn on to charge capacitor C_2 with V_o. The voltage across C_2 is then used to supply power to the high-side gate driver.

4.4.2 TX control circuit

To detect the effect of load modulation on the TX side, the compensation capacitor C_1 voltage V_C is rectified and low-pass filtered as shown in Fig. 11. The measured voltage v_{cr} in effect measures Q factor of the TX resonant tank. The amplitude of v_{cr} can be expressed

as:

$$V_{cr} = H_o V_c = Q_1 H_o V_{sw1}, \tag{4.16}$$

where:

$$H_o = \frac{R_6}{R_5 + R_6}. \tag{4.17}$$

Therefore, the amplitude of the voltage v_{cr} is proportional to the quality factor of the tank and can be used to detect load modulation on the TX side.

The control circuit employed in TX is shown in Fig. 4.12. At the start of the period, the SR latch is set which turns on the TX and the TX transmits power. When the output voltage reaches a high threshold V_H, the switch S_{RX} is turned off. The switch turn off increases the quality factor of TX resonant tank, Q, which is detected by rectifying and low-pass filtering TX compensation capacitor C_1 voltage V_c as shown in Fig. 4.12. The voltage v_{cr} increases against a reference V_{ref} which resets the latch on the TX side and turns off TX until the next cycle.

As explained in Section 4.2, the maximum amplitude of the capacitor C_1 voltage V_{CH} remains constant regardless of distance and load variations. Therefore, a fixed voltage reference V_{ref} can be used for all TX-RX distances to determine whether the RX is on or off in the TX control circuit.

Finally, it is noted that the rectifier design at 6.78MHz to detect capacitor C_1 voltage can be very challenging. The rectification capacitor C_3 should be small enough to not significantly alter the TX tank resonant frequency. Therefore, the rectification capacitor C_3 is chosen to be 10pF ($\sim$30x smaller than C_1). A small rectification capacitor forms a capacitive divider with the diode D_t junction capacitance ($\sim$5pF). Since high-frequency ac voltage amplitude across the capacitor C_1 is very large ($\sim$500V), a significant high-frequency voltage signal appears at the output of the rectifier and makes the load modulation detection very difficult. The problem is circumvented by merging low-pass filter into the rectifier by introducing a resistor R_3. This significantly reduces high-frequency coupling at the output of the rectifier and allows the controller to accurately determine RX on/off states. The low

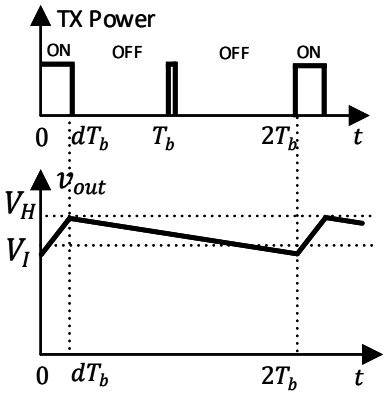

Figure 4.13: Circuit operation under light load conditions.

pass filter corner frequency for the first and second stage ($\frac{1}{2\pi R_3 C_3}$, $\frac{1}{2\pi R_4 C_4}$) is selected to be 40x smaller than the 6.78MHz to significantly reduce the high-frequency signal amplitude while allowing low frequency modulated signal to appear at the output v_{cr}.

4.5 Light load operation

The circuit can maintain high efficiency under light load conditions and regulates output voltage from full load to no load. To maintain high efficiency under light load conditions, the TX turns on only when RX needs power. An example case for circuit output waveforms under light load condition is shown in Fig. 4.13. The TX turn on charges the output capacitor and increases the output voltage v_{out}. When v_{out} reaches high threshold V_H, RX switch S_{RX} turns off which turns off the TX. The output capacitor starts to discharge. When the next period arrives, since the light load is connected to the output capacitor, the output voltage is still higher than the V_I. Thus, the RX switch S_{RX} is off. When TX turns on, it detects that the RX switch S_{RX} is is off and it turns off as well. The operation repeats afterward. Therefore, the TX only turns on when RX needs power which increases the system efficiency.

4.6 Experimental validation

Wireless power transfer for biomedical implants is generally designed to operate in MHz frequencies [49, 50, 45, 53, 54]. Operating in kHz frequencies results in a lower Q factor of coils. While the Q factor of coils can be increased by using Litz wire and coupling coefficient can be enhanced by using ferrite cores, both result in bulky coils. Operation in the MHz regime increases the Q factor of the coils and simple air-core coils can be utilized resulting in lightweight coils [55]. Therefore, 6-turn air-core coils are used for the prototype. The parameters of coils used in the prototype circuit are listed in Table 4.2.

A 330mW prototype circuit shown in Fig. 4.16(b) was built and the proposed controller is implemented. Components used to build the circuit are listed in Table 4.2. TX and RX coils are designed to be of equal diameter (3cm) to remain within geometrical constraints of the implant while maximizing the coupling coefficient [56]. The circuit was designed to operate at 6.78MHz to remain within the ISM band. EPC8004 GaN FETs are used to make the half-bridge circuit in TX. Their low output capacitance allows operation at 6.78MHz. The burst-mode frequency (f_b) is selected to be 1.5kHz.

Experimental waveforms of the circuit are shown in Fig. 4.14. Figures 4.14(a-c) show TX control signal v_{cr} (ref. Fig. 4.12) and output voltage v_{out} at full load condition (330mW) when the TX and RX distance is 1cm, 2cm, and 3cm, respectively. Turn on of the TX increases the output voltage. When the output voltage reaches a high threshold, RX turns S_{RX} off which causes the TX to turn off as well until the next period. TX control voltage v_{cr} indicates how the TX detects the presence of RX. As discussed in Section 4.2, when the RX is receiving power, S_{RX} is on and quality factor of the tank is low ($Q_{1,on}$) which results in lower v_{cr} as can be seen from Eq. (4.16). When the RX switch S_{RX} turns off, the quality factor of the tank increases ($Q_{1,off}$) which results in an instant increase in voltage v_{cr} indicated by Δv_{cr} in Fig. 4.14(a). It is compared with V_{ref} on TX controller and the TX is correspondingly turned off which decreases the voltage v_{cr} to zero. The TX is turned on in the next period and the process is repeated. Figure 4.14(d) shows the zoomed view of

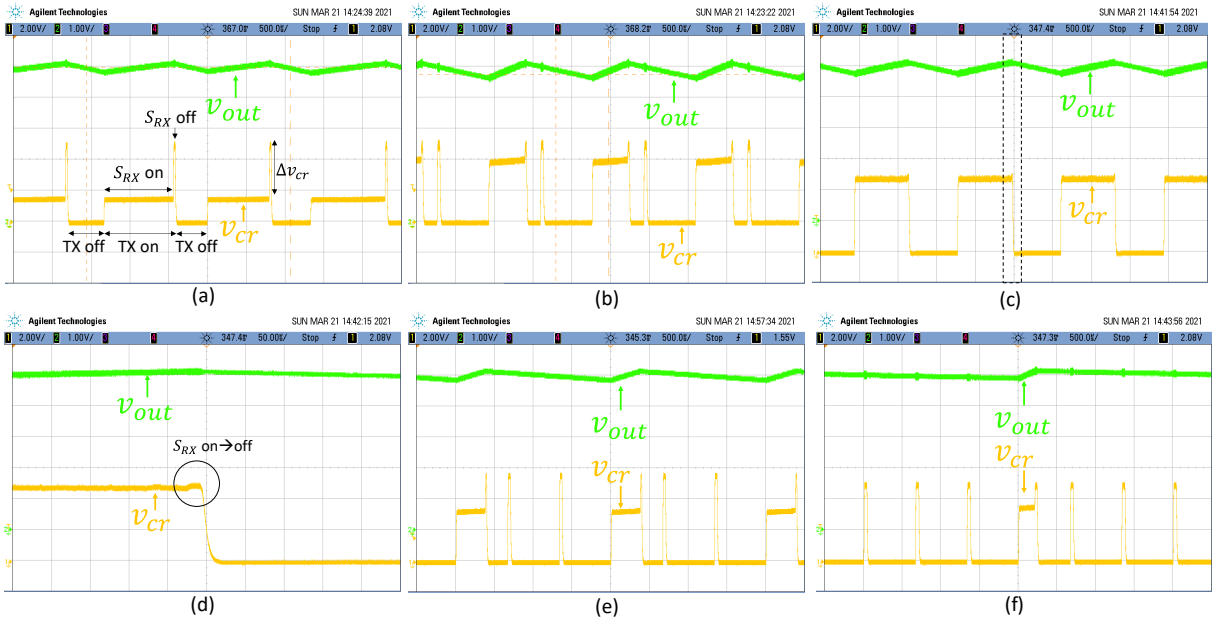

Figure 4.14: Experimental waveforms for full-load condition (330mW) when TX and RX distance is (a) 1cm, (b) 2cm, (c) 3cm and (d) zoomed view of (c) to show detection of SRX on to off transition on TX controller. Experimental waveform for light-load condition (e) 128mW and (f) 33mW when the TX and RX distance is 2cm.

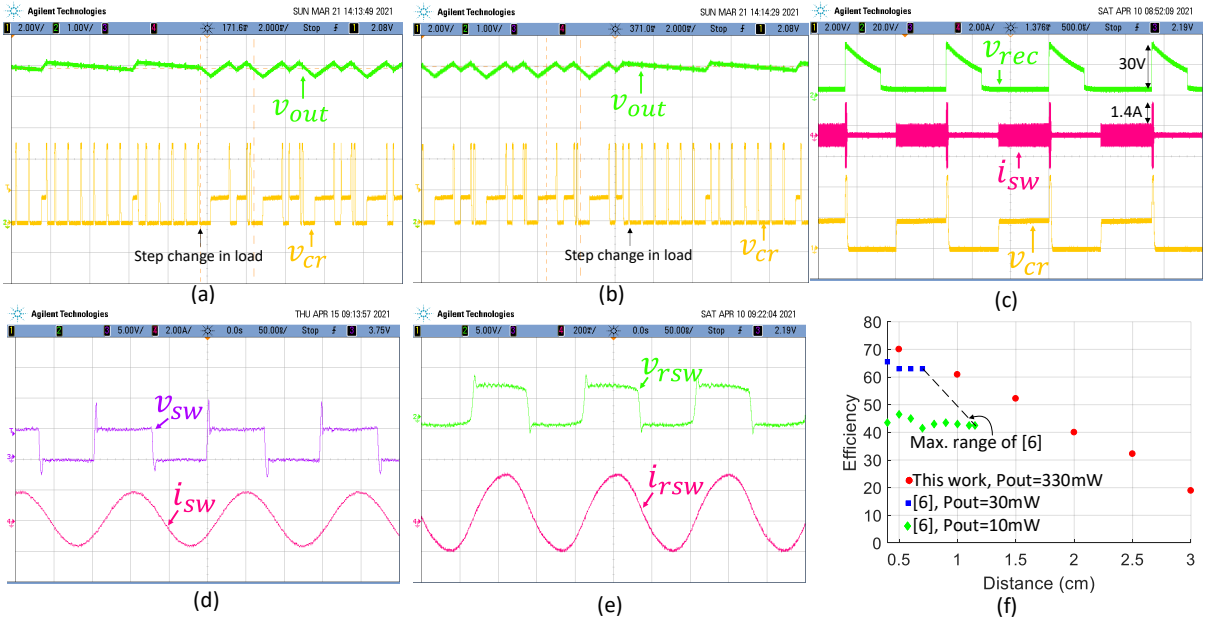

Figure 4.15: Dynamic response of the circuit as load instantaneously changes from (a) 33mW to 330mW and (b) 330mW to 33mW when TX and RX distance is 1cm. (c) Voltage spikes at the output of diode bridge rectifier and current change in TX coil, (d) TX switch node voltage and current, (e) RX switch node voltage and current and (f) End-to-end system efficiency for 330mW load.

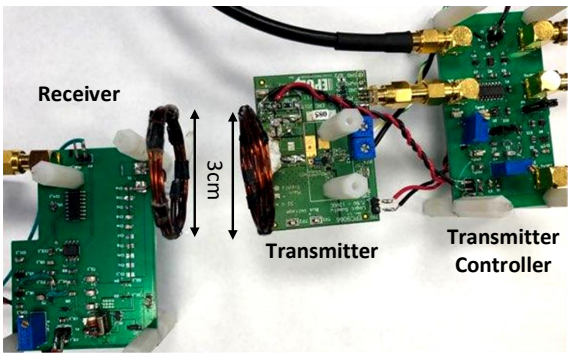

Figure 4.16: Experimental setup.

Fig. 4.14(c) to show the voltage v_{cr} change when the RX switch S_{RX} transitions from on to off state. A slight change in the voltage can be observed which results in TX detecting the load modulation. This also indicates that the maximum separation between TX and RX can be 3cm after which the TX can not detect load modulation and output voltage starts to decrease.

Figures 4.14(e, f) illustrate the light load operation of the circuit (128mW and 33mW) as described in Section 4.5. It can be observed in most cases the TX turns on and off right away (indicated by v_{cr}), as the light load is connected at the output and ($V_{out} > V_I$).

The dynamic response of the circuit when load power changes from 33mW to 330mW and from 330mW to 33mW is shown in Fig. 4.15(a, b). It can be observed that the circuit output voltage remains well-regulated during the load transients. Voltage spikes at the output of the rectifier v_{rec} and current change in the TX coil when the RX switch S_{RX} turns on and off are shown in Fig. 4.15(c). Even though the voltage spike is 30V, the Zener diode Z_r protects the switch S_{RX} from overvoltage breakdown. Furthermore, the current in the TX tank and switches increases to the value of the unloaded TX tank. Figure 4.15(d) shows the TX half-bridge switch node voltage v_{sw} and current i_{sw} (ref. Fig. 4.9(a)). It can be observed that the TX achieves zero-voltage switching (ZVS) as the current i_{sw} lags the switch node voltage v_{sw} and the switch node voltage has a smooth rise and fall transitions. RX coil current i_{rsw} and diode bridge voltage v_{rsw} (ref. Fig. 4.9(a)) is shown in Fig. 4.15(e). The power transfer efficiency of the circuit w.r.t. distance when full load is connected to the output (330mW) is

Table 4.2: COMPONENTS USED IN THE WPT SYSTEM.

TX Coil	$L_1 = 1.85\,\mu H$, $Q_1 = 135$, dia = 3cm, 6 turn
TX compensation capacitor (C_1)	298pF
RX Coil	$L_2 = 1.98\,\mu H$, $Q_2 = 135$, dia = 3cm, 6 turn
RX compensation capacitor (C_2)	278pF
Switch ($S_{1,2}$)	EPC8004
Gate driver for Switch ($S_{1,2}$)	LM5113TME
Switch (S_{RX})	IRLML0060 TRPBF
Gate driver for Switch (S_{RX})	UCC27201D
RX diode (D)	RB520CM-60T2R
RX Zener diode (Z_t)	MMSZ5258, 36V Zener diode
TX controller diode (D_t)	BAS40-02V-V-G
Capacitors (C_{out})	$220\,\mu F$, 1210

shown in Fig. 4.15(f). The power transfer efficiency ranges from 70.0% at TX-RX distance of 0.5 cm to 19% at TX-RX distance of 3cm. The system efficiency is high when TX and RX are close. It decreases as the distance between TX and RX is increased which decreases the coupling coefficient and the reflected load impedances (R_2', R_d', R_e'). This results in increased TX current and increased loss in R_1, R_2' and R_d'. A comparison of the proposed system efficiency w.r.t. distance with [45] is also provided.

A comparison of the proposed WPT system with state-of-the-art WPT systems is shown in Table III. To the left of our work, WPT systems operating at fixed frequency are listed. Among the systems, our work achieves the best peak efficiency and largest normalized range (normalized max range is defined as max. range divided by geometric mean of TX and RX coils diameter [49]). To the right of our work, WPT systems operating at variable frequency are listed. These systems achieve even higher efficiency and range, but the maximum power that can be delivered is limited to 94mW to remain within the FCC limits [50].

Table 4.3: PERFORMANCE COMPARISON WITH STATE-OF-THE-ART.

	[57] ISSCC' 15	[53] JSSC' 15	[45] JSSC' 18	[46] ISSCC' 21	This work	[49] ISSCC' 17	[50] JSSC' 19
Frequency (MHz)	13.56	13.56	13.56	6.78	6.78	10.4-13.56	1.7-30
Output power (mW)	234	102	30	32	330	18	93.8
TX coil dia. (d_{TX})	5cm	2.5cm	2.52cm	3.2cm	3cm	3cm	3cm
RX coil dia. (d_{RX})	0.95cm	0.95cm	2cm	2.5cm	3cm	3cm	3cm
Max. efficiency (@ d_{TX-RX})	62.4% (3mm)	50% (3mm)	67% (3mm)	61.9% (6.5mm)	70.0% (5mm)	73.7% -	80.1% -
Max. distance	1.8cm‡	-	0.7cm	-	3cm	4.2cm	4.2cm
Normalized range†	0.82	-	0.3	-	1	1.4	1.4
Total coils	3	3	3	2	2	2	2

†Normalized range = $\frac{Max\ distance}{\sqrt{d_{TX}d_{TX}}}$

‡The system achieved 1.8cm range with 50mW output power and 0.3cm range with 234mW output power.

4.7 Conclusion

A burst-mode controlled inductive wireless power transfer system is presented in this paper. Power is transmitted in bursts between the transmitter (TX) and receiver (RX). The duty cycle of the burst is controlled through load modulation to control power flow between TX and RX. The proposed WPT circuit exhibits immunity to distance up to 3cm TX-RX separation and load variations from full load to no load. No extra communication channel is present to establish feedback between transmitter and receiver, making the circuit suitable for many applications. A 330-milliwatt prototype circuit to charge a 280mAh battery for use in a medical implant is designed, built, and tested.

CHAPTER 5

Research Contributions and Future Work

5.1 Summary of research contributions

This thesis advances state-of-art in the area of power transfer techniques for biomedical implants. Three major contributions of the thesis include:

5.1.1 Wired power transfer between distributed modules of a biomedical implant

The first part of the thesis introduced a resonant inverter architecture appropriate for wired power transfer between distributed modules of a biomedical implant. A T-LCC resonant converter is identified as a suitable topology for wired power transfer between distributed modules of a biomedical implant. This thesis presents an analysis and design methodology to realize the converter. The proposed resonant network achieved:

- low output impedance which allows it to regulate output voltage against wide load variation without closed-loop control.
- high efficiency by minimizing circulating current losses and maintaining soft-switching across a wide load range.
- small form factor by minimizing inductors.
- conversion ratio greater than unity by using resonant properties of the network.
- zero DC output voltage which prevents static electric field between adjacent conductors.

A 130-mW, 1-MHz prototype T-LCC resonant inverter achieved a full power efficiency of 86% and maintained efficiency above 80% across a two-to-one power range. Furthermore, the converter achieved a power density of 12W/in^3, while only having a 2.8% variation in output voltage across full load variation.

5.1.2 Leadless and batteryless wirelessly powered intravenous cardiac pacemaker

The second part of the thesis introduced a leadless and batteryless, wirelessly powered intravenous cardiac pacemaker. Traditional lead-based cardiac pacemakers suffer from lead-related complications which include lead fracture, lead dislodgement, and venous obstruction. Modern leadless pacemakers mitigate the complications, but, since they are implanted inside the heart with a small battery, their limited battery lifetime necessities device replacement within the patient's lifetime.

The research advances state-of-the-art by significantly reducing the power consumption and improving stimulation pulse characteristics as compared to state-of-art leadless and batteryless, wirelessly powered pacemaker [4]. The pacemaker proposed in [4] consumes 1W of power which can deplete 1Ah battery in 3.6 hours and would be impractical for use by patients. High transmitted power also makes the system incompliant with FCC SAR regulations. Furthermore, it can only apply a 3.5V amplitude pulse with a maximum pulse period of 300 µs which is insufficient to cover a broad range of complications in different patients. Lastly, the pacemaker does not do active charge neutralization which can damage tissue in long run.

The proposed pacemaker circuit achieved the following:

- The RX circuit power consumption is significantly reduced by transmitting power at low frequency and turning it on only for the duration the stimulation is applied. Stimulating in bursts (duty cycle:0.05%) reduces power consumption by 2000x as compared to continous power transmission. This allows the pacemaker to operate from a 280mAh

battery for 1.4 months.

- The RX circuit can apply 5V/5mA stimulation with a programmable pulse period (including 1msec) which allows it to cover a range of patients, as typically done by traditional pacemakers [20].
- The RX circuit achieves active charge neutralization without using a large decoupling capacitor which miniaturizes the implant.
- The pacemaker achieved a small form factor of $15\times\pi\times2.25\text{mm}^3$ by minimizing off-chip components.
- The proposed pacemaker is complaint with FCC and IEEE SAR regulations.

The prototype pacemaker circuit applied monophasic, cathodic, and current/voltage stimulation to the heart with a programmable pulse period. It consumed 1mW power for a 0.5msec stimulation pulse, which qualifies for pacemaker application. 5V voltage and 5mA current stimulation over 2.5cm TX and RX distance with controllable pulse width and pulse frequency is demonstrated. Stimulation of the porcine heart validated the pacemaker functionality.

5.1.3 Wireless power transfer for a biomedical implant

The third part of the thesis introduced a burst-mode controlled inductive wireless power transfer system. The proposed WPT system:

- regulates output voltage against large distance and load variations.
- eliminates back-channel communication link between TX and RX by using the inherent load reflection property of WPT circuits.
- achieves high efficiency by only using a switch to regulate load power and removing power stages including DC/DC converters in the WPT circuit. Furthermore, TX power is transmitted only for the duration that RX needs power.

- transmits power at a fixed frequency to remain within the ISM band and overcome the power limit of varying frequency WPT circuits.

A 330-milliwatt prototype circuit to charge a 280mAh battery for use in a medical implant is designed, built, and tested. The proposed WPT circuit achieved an efficiency of 70.0% at 5mm TX-RX seperation, regulates output voltage up to 3cm TX-RX separation and load variations from full load to no load.

5.2 Future work

The research advances state-of-the-art by mitigating lead and battery-related limitations of commercial pacemakers, but the following major challenges remain:

5.2.1 Device assembly

For the device to be practically viable, the device assembly needs to be improved. The device must be assembled such that it is hollow from inside and electronics are contained in the periphery. The device must be packaged in a biocompatible polymer such as Parylene and the device implantation lifetime must exceed that of leadless pacemakers. Furthermore, device flexibility must be improved to ease device implantation using a catheter or similar minimally invasive approach.

5.2.2 Closed-loop pacemaker

Modern pacemakers sense the heart signals and stimulate if the inherent heartbeat is missing or delayed. This reduces the need for external pacing. Furthermore, modern pacemakers use rate-responsive techniques to adjust the heartbeat if a patient is doing an exercise.

The proposed pacemaker applies open-loop stimulation to the heart and cannot sense heart signals. The pacemaker capabilities can be enhanced by integrating sensing and communication capabilities in it. The stimulation module can sense heart signals and commu-

nicate them back to the subcutaneous module. The subcutaneous module can process the received signals and apply stimulation accordingly. This would allow the pacemaker to work in a closed-loop manner and provide much improved therapy to the patients.

5.2.3 Biventricular pacemaker

Biventricular pacemakers are used for cardiac resynchronization therapy. Biventricular pacemakers require 3 leads from a standard lead-based pacemaker. Multiple leads increase the likelihood of lead-related complications. Modern leadless and battery-based pacemakers [Micra [20], Nanostim [58]] are single-chamber pacemakers and can not be used for biventricular pacing. There is no telemetry present between different leadless pacemakers to synchronize them. Integrating telemetry capabilities would reduce their battery life significantly. Furthermore, the metal encapsulation of the pacemakers further limits their telemetry capabilities.

The proposed pacemaker seems to be a very good fit for the application. Multiple stimulation modules can be employed to sense and pace in different chambers of the heart. One master subcutaneous module can easily communicate with and control multiple stimulation modules. Furthermore, cardiac resynchronization therapy requires 100% pacing. Lead-based and leadless pacemakers that contain a battery have a limited lifetime under such aggressive pacing needs. Since the proposed pacemaker is wirelessly powered from an external module with a rechargeable battery, the lifetime can be increased.

References

[1] R. S. Frederieke Elsinger and A. Spijkerboer, *Cardiovascular devices on Chest X-Ray*, 2018 (accessed November 20, 2020). [Online]. Available: https://radiologyassistant.nl/cardiovascular/devices/cardiovascular-devices

[2] L. S. Y. Wong, S. Hossain, A. Ta, J. Edvinsson, D. H. Rivas, and H. Naas, "A very low-power CMOS mixed-signal IC for implantable pacemaker applications," *IEEE Journal of Solid-State Circuits*, vol. 39, no. 12, pp. 2446–2456, 2004.

[3] S. Lee, M. Y. Su, M. Liang, Y. Chen, C. Hsieh, C. Yang, H. Lai, J. Lin, and Q. Fang, "A programmable implantable microstimulator soc with wireless telemetry: Application in closed-loop endocardial stimulation for cardiac pacemaker," *IEEE Transactions on Biomedical Circuits and Systems*, vol. 5, no. 6, pp. 511–522, 2011.

[4] H. Lyu, P. Gad, H. Zhong, V. R. Edgerton, and A. Babakhani, "A 430-MHz wirelessly powered implantable pulse generator with intensity/rate control and sub-1 μa quiescent current consumption," *IEEE Transactions on Biomedical Circuits and Systems*, vol. 13, no. 1, pp. 180–190, 2019.

[5] P. Gutruf, R. Yin, K. B. Lee, and et al., "Wireless, battery-free, fully implantable multimodal and multisite pacemakers for applications in small animal models," *Nature Communication*, 2019.

[6] S. Knisley, W. Smith, and R. Ideker, "Effect of intrastimulus polarity reversal on electric field stimulation thresholds in frog and rabbit myocardium," *Journal of Cardiovascular Electrophysiology*, vol. 3, pp. 239–254, 1992.

[7] D. Rozgic, V. Hokhikyan, W. Jiang, S. Basir-Kazeruni, H. Chandrakumar, W. Leng, and D. Markovic, "A true full-duplex 32-channel 0.135cm^3 neural interface," in *2017 IEEE Biomedical Circuits and Systems Conference (BioCAS)*, 2017, pp. 1–4.

[8] D. Rozgic, V. Hokhikyan, W. Jiang, I. Akita, S. Basir-Kazeruni, H. Chandrakumar, and D. Markovic, "A 0.338cm^3, artifact-free, 64-contact neuromodulation platform for simultaneous stimulation and sensing," *IEEE Transactions on Biomedical Circuits and Systems*, vol. 13, no. 1, pp. 38–55, 2019.

[9] A. K. RamRakhyani, S. Mirabbasi, and M. Chiao, "Design and optimization of resonance-based efficient wireless power delivery systems for biomedical implants," *IEEE Transactions on Biomedical Circuits and Systems*, vol. 5, no. 1, pp. 48–63, 2011.

[10] J. Pan, A. A. Abidi, D. Rozgic, H. Chandrakumar, and D. Markovic, "An inductively-coupled wireless power-transfer system that is immune to distance and load variations," in *2017 IEEE International Solid-State Circuits Conference (ISSCC)*, 2017, pp. 382–383.

[11] C. Polk and E. Postow, *Handbook of biological effects of electromagnetic fields*, 2nd ed. CRC press, 1996.

[12] I. Batarseh, "Resonant converter topologies with three and four energy storage elements," *IEEE Transactions on Power Electronics*, vol. 9, no. 1, pp. 64–73, 1994.

[13] M. Prabhakar, S. Arulmozhi, and V. Kamaraj, "Selection criteria and analysis of LCC resonant DC–DC converters for automotive applications," *Modern Applied Science*, vol. 3, no. 7, 2009.

[14] M. Prabhakar and V. Kamaraj, "Optimal design and implementation of LCC resonant converter for automotive application," in *2010 4^{th} International Power Engineering and Optimization Conference (PEOCO)*, 2010, pp. 507–510.

[15] R. Erickson and D. Maksimovic, *Fundamentals of Power Electronics*, 2nd ed. Springer, 2001.

[16] H. G. Mond and A. Proclemer, "The 11th world survey of cardiac pacing and implantable cardioverter-defibrillators: Calendar year 2009-a world society of arrhythmia's project," *Pacing and clinical electrophysiology : PACE*, vol. 34, no. 8, pp. 1013–1027, 2011.

[17] F. V. Tjong and V. Y. Reddy, "Permanent leadless cardiac pacemaker therapy," *Circulation*, vol. 135, no. 15, pp. 1458–1470, 2017.

[18] N. Bhatia and M. El-Chami, "Leadless pacemakers: a contemporary review," *Journal of geriatric cardiology*, vol. 15, pp. 249–253, 2018.

[19] S. Lee, C. Cheng, and M. Liang, "A low-power bidirectional telemetry device with a near-field charging feature for a cardiac microstimulator," *IEEE Transactions on Biomedical Circuits and Systems*, vol. 5, no. 4, pp. 357–367, 2011.

[20] Medtronic, *Micra Transcatheter Pacing System*, (accessed February 16, 2021). [Online]. Available: https://www.medtronic.me/content/dam/medtronic-com/01_crhf/brady/pdfs/2018-05-micra-specification-sheet.pdf

[21] K. Ellenbogen, B. L. Wilkoff, G. N. Kay, C. Lau, and A. Auricchio, *Clinical cardiac pacing, Defibrillation and Resynchronization Therapy*, 4th ed. Elsevier Health Sciences, 2011.

[22] K. Ellenhogen and M. Wood, Eds., *Cardiac pacing and ICDs*, 1st ed. Wiley, 2005.

[23] J. Webster, Ed., *Design of Cardiac Pacemakers*, 1st ed. New York, New York, USA: IEEE Press, 1995.

[24] K. S. J. N. Weiss, Q. Zhilin, "Electrophysiology of hypokalemia and hyperkalemia," *Circulation: Arrhythmia and Electrophysiology*, 2017.

[25] W. Irnich, "The chronaxie time and its practical importance." in *Pacing and clinical electrophysiology : PACE*, 1980, pp. 292–301.

[26] G. Kovacs, *Introduction to the Theory, Design and Modeling of Thin-Film Microelectrodes for Neural Interfaces*, 4th ed., D. Stenger and T. McKenna, Eds. Academic Press, 1994.

[27] W. Franks, I. Schenker, P. Schmutz, and A. Hierlemann, "Impedance characterization and modeling of electrodes for biomedical applications," *IEEE Transactions on Biomedical Engineering*, vol. 52, no. 7, 2005.

[28] K. Arunachalam, "Coronary sinus anatomy and its importance-evidence based review," *Anatomy and Physiology: Current research*, vol. 6, no. 2, 2016.

[29] P. S. Rahko, "Evaluation of the skin-to-heart distance in the standing adult by two-dimensional echocardiography," *Journal of the American Society of Echocardiography*, vol. 21, no. 6, pp. 761 – 764, 2008.

[30] Quallion, *Quallion 280mAh Cell.*, (accessed June 01, 2021). [Online]. Available: https://www.dropbox.com/sh/6yf63f2sq0gbiub/AADToD4WsWTrTNLvsttqsHea?dl=0

[31] M. Biffi, J. Sperzel, C. Martignani, A. Branzi, and G. Boriani, "Evolution of pacing for bradycardia autocapture," *European Heart Journal Supplements*, vol. 9, pp. 123–132, 12 2007.

[32] G. Dandamudi and P. Vijayaraman, "How to perform permanent HIS bundle pacing in routine clinical practice," *Heart Rhythm*, vol. 13, no. 6, pp. 1362–1366, 06 2016.

[33] L. Gu, G. Zulauf, A. Stein, P. A. Kyaw, T. Chen, and J. M. R. Davila, "6.78MHz wireless power transfer with self-resonant coils at 95% dc–dc efficiency," *IEEE Transactions on Power Electronics*, vol. 36, no. 3, pp. 2456–2460, 2021.

[34] U. Anwar, Z. Liu, and D. Markovic, "A burst-mode controlled inductive wireless power transfer system," in *2020 IEEE 21st Workshop on Control and Modeling for Power Electronics (COMPEL)*, 2020, pp. 1–6.

[35] S. Y. R. Hui, W. Zhong, and C. K. Lee, "A critical review of recent progress in mid-range wireless power transfer," *IEEE Transactions on Power Electronics*, vol. 29, no. 9, pp. 4500–4511, 2014.

[36] H. M. Lee, H. Park, and M. Ghovanloo, "A power-efficient wireless system with adaptive supply control for deep brain stimulation," *IEEE Journal of Solid-State Circuits*, vol. 48, no. 9, pp. 2203–2216, 2013.

[37] M. Ghovanloo and K. Najafi, "Fully integrated wideband high-current rectifiers for inductively powered devices," *IEEE Journal of Solid-State Circuits*, vol. 39, no. 11, pp. 1976–1984, 2004.

[38] C. Huang, T. Kawajiri, and H. Ishikuro, "A 13.56MHz wireless power transfer system with enhanced load-transient response and efficiency by fully integrated wireless constant-idle-time control for biomedical implants," *IEEE Journal of Solid-State Circuits*, vol. 53, no. 2, pp. 538–551, 2018.

[39] E. Adair and R. Petersen, "Biological effects of radiofrequency/microwave radiation," *IEEE Transactions on Microwave Theory and Techniques*, vol. 50, no. 3, pp. 953–962, 2002.

[40] S. Y. R. Hui, "Past, present and future trends of non-radiative wireless power transfer," *CPSS Transactions on Power Electronics and Applications*, vol. 1, no. 1, pp. 83–91, 2016.

[41] W. Zhong and S. Y. R. Hui, "Maximum energy efficiency operation of series-series resonant wireless power transfer systems using on-off keying modulation," *IEEE Transactions on Power Electronics*, vol. 33, no. 4, pp. 3595–3603, 2018.

[42] W. Zhong, H. Li, H. Cui, S. Y. R. Hui, and D. Xu, "Maximum-efficiency operation of a 3.7kw inductive wireless charging system by using on-off keying modulation," in *2018 IEEE Energy Conversion Congress and Exposition (ECCE)*, 2018, pp. 921–927.

[43] R. Mai, Y. Liu, Y. Li, P. Yue, G. Cao, and Z. He, "An active-rectifier-based maximum efficiency tracking method using an additional measurement coil for wireless power transfer," *IEEE Transactions on Power Electronics*, vol. 33, no. 1, pp. 716–728, 2018.

[44] D. Ahn, S. Kim, J. Moon, and I. Cho, "Wireless power transfer with automatic feedback control of load resistance transformation," *IEEE Transactions on Power Electronics*, vol. 31, no. 11, pp. 7876–7886, 2016.

[45] C. Huang, T. Kawajiri, and H. Ishikuro, "A 13.56-MHz wireless power transfer system with enhanced load-transient response and efficiency by fully integrated wireless constant-idle-time control for biomedical implants," *IEEE Journal of Solid-State Circuits*, vol. 53, no. 2, pp. 538–551, 2018.

[46] J. Tang, L. Zhao, and C. Huang, "A wireless power transfer system with up-to-20% light- load efficiency enhancement and instant dynamic response by fully integrated wireless hysteretic control for bioimplants," in *2021 IEEE International Solid- State Circuits Conference (ISSCC)*, vol. 64, 2021, pp. 470–472.

[47] W. X. Zhong and S. Y. R. Hui, "Maximum energy efficiency tracking for wireless power transfer systems," *IEEE Transactions on Power Electronics*, vol. 30, no. 7, pp. 4025–4034, 2015.

[48] P. Si, A. P. Hu, S. Malpas, and D. Budgett, "A frequency control method for regulating wireless power to implantable devices," *IEEE Transactions on Biomedical Circuits and Systems*, vol. 2, no. 1, pp. 22–29, 2008.

[49] J. Pan, A. A. Abidi, D. Rozgić, H. Chandrakumar, and D. Marković, "An inductively-coupled wireless power-transfer system that is immune to distance and load variations," in *2017 IEEE International Solid-State Circuits Conference (ISSCC)*, 2017, pp. 382–383.

[50] J. Pan, A. A. Abidi, W. Jiang, and D. Marković, "Simultaneous transmission of up to 94-mW self-regulated wireless power and up to 5-Mb/s reverse data over a single pair of coils," *IEEE Journal of Solid-State Circuits*, vol. 54, no. 4, pp. 1003–1016, 2019.

[51] R. Erickson and D. Maksimovic, *Fundamentals of Power Electronics*, 2nd ed. Springer, 2001.

[52] S. Y. R. Hui, W. Zhong, and C. K. Lee, "A critical review of recent progress in mid-range wireless power transfer," *IEEE Transactions on Power Electronics*, vol. 29, no. 9, pp. 4500–4511, 2014.

[53] X. Li, C. Tsui, and W. Ki, "A 13.56MHz wireless power transfer system with reconfigurable resonant regulating rectifier and wireless power control for implantable medical devices," *IEEE Journal of Solid-State Circuits*, vol. 50, no. 4, pp. 978–989, 2015.

[54] H. M. Lee and M. Ghovanloo, "An adaptive reconfigurable active voltage doubler/rectifier for extended-range inductive power transmission," in *2012 IEEE International Solid-State Circuits Conference*, 2012, pp. 286–288.

[55] L. Gu, G. Zulauf, A. Stein, P. A. Kyaw, T. Chen, and J. M. R. Davila, "6.78MHz wireless power transfer with self-resonant coils at 95% DC–DC efficiency," *IEEE Transactions on Power Electronics*, vol. 36, no. 3, pp. 2456–2460, 2021.

[56] B. R. Long, J. M. Miller, A. Daga, P. C. Schrafel, and J. Wolgemuth, "Which way for wireless power: High Q or high k?" in *2016 IEEE PELS Workshop on Emerging Technologies: Wireless Power Transfer (WoW)*, 2016, pp. 6–10.

[57] X. Li, C. Tsui, and W. Ki, "Wireless power transfer system using primary equalizer for coupling- and load-range extension in bio-implant applications," in *2015 IEEE International Solid-State Circuits Conference*, 2015, pp. 1–3.

[58] J. Sperzel, C. Hamm, and A. Hain, "Nanostim-leadless pacemaker," in *Herzschrittmachertherapie und Elektrophysiologie*, vol. 29, no. 4, 2018, pp. 327–333.